Development of Spectral Microscopy Imaging Technique for Time-Resolved Imaging of Primary Breakup in High-Pressure Fuel Sprays

A Thesis

Presented to

The academic faculty

By

Yoontak Kim

In Partial Fulfillment
of the Requirements for the Degree
Master of Science in the
School of George W. Woodruff School of Mechanical Engineering

Georgia Institute of Technology

December 2017

Development of Spectral Microscopy Imaging Technique for Time-Resolved Imaging of Primary Breakup in High-Pressure Fuel Sprays

Approved by:

Dr. Caroline Genzale, Advisor

George W. Woodruff School of Mechanical Engineering

Georgia Institute of Technology

Dr. Todd Sulchek

George W. Woodruff School of Mechanical Engineering

Georgia Institute of Technology

Dr. Oleksandr (Sasha) Bibik

School of Aerospace Engineering Georgia Institute of Technology

Georgia Institute of Technology

Date Approved: October 2017

TABLE OF CONTENTS

LIST OF FIGURES

LIST OF TABLES

INTRODUCTION

1. Background

Global warming has been drawing attention around the world recently, suggesting that a new focus of engineering should be on greenhouse gas emissions. Environmental organizations such as the EPA have been modifying their policies accordingly, which encourage researchers to seek cleaner energy solutions [1]. One of the main culprits of global warming greenhouse gas is carbon dioxide. According to the EPA [2], the transportation sector is the second largest source of CO_2, and the largest source of CO, which is not only toxic but also readily reactive with O_2 to form CO_2. In response to this problem, automotive companies such as Tesla and Volvo are rapidly designing electric vehicles. Although electric vehicles are gaining attention, their actual sales are expected to be less than 6% of all vehicle sales by 2040 [3]. A more reasonable response could be producing a more efficient internal combustion engine. The Department of Energy acknowledges the significance of internal combustion engine vehicles and states “Improving the efficiency of internal combustion engines is one of the most promising and cost-effective near- to mid-term approaches to increasing highway vehicles' fuel economy” [4].

One method for improving the efficiency of the engine is to focus on the fuel injector and studying its spray physics, as combustion starts with preparing the air-fuel mixture. Direct injection technologies such as diesel and gasoline direct injection (GDI) engines have better efficiency because they have closer control over fuel mixture and they don’t require throttles [5]. Direct injection is the spraying of highly pressurized fuel into the compressed engine cylinder, which leads to the near-instant breakup, or atomization, of the fuel, fuel vaporization, and combustion. However, the fundamental physics that govern fuel atomization at engine conditions are not yet

thoroughly understood, which results from the difficulty of visualizing real fuel injection processes. In a direct-injection engine, the fuel breakup features length is expected to be larger than 1 μm [6], moving at a speed of less than 620 m/s according to Bernoulli's equation.

Imaging such a flow requires extremely high temporal and the spatial resolutions. For digital cameras, the sensor pixel size must, at a minimum, behalf of the smallest image feature of interest, according to the Nyquist criterion. Typical scientific-grade high-speed cameras have pixel sizes of about 20 μm; that is, the magnification factor of the lens needs to exceed 40 to visualize 1 μm object. At these magnifications and at flow speeds of hundreds of m/s, the required exposure time scale to effectively freeze the flow motion is on the order of nanoseconds, with framing rates of mega frames per second to properly capture flow evolution. Even with current state-of-the-art equipment, the requirements are relatively prohibitive. To circumvent the requirements, most engine spray research [7, 8, 9, 10, 11, 12] has studied lower pressure injections, far downstream spray regions where velocities have decayed, the use of time-averaged images, or a combination of the three.

Two different models have been proposed in the literature to provide a description of the initial breakup, or primary breakup, of high-pressure liquid fuel: 1) the model based on that liquid turbulence properties drive primary breakup, and 2) the model based on that aerodynamic forces that arise due to liquid-gas velocity differentials drive primary breakup. The aerodynamic breakup model was introduced by Reitz and coworkers [7, 8], based on measurements of large-scale spray characteristics such as the time-averaged spray spreading angle. The turbulence-induced breakup model was introduced by Faeth and coworkers, based on direct imaging of the liquid-gas interface of low-velocity turbulent round liquid jets with holography [9, 10]. A comparison of the primary breakup scales, or characteristic diameter of the initial droplets formed, predicted by the model of

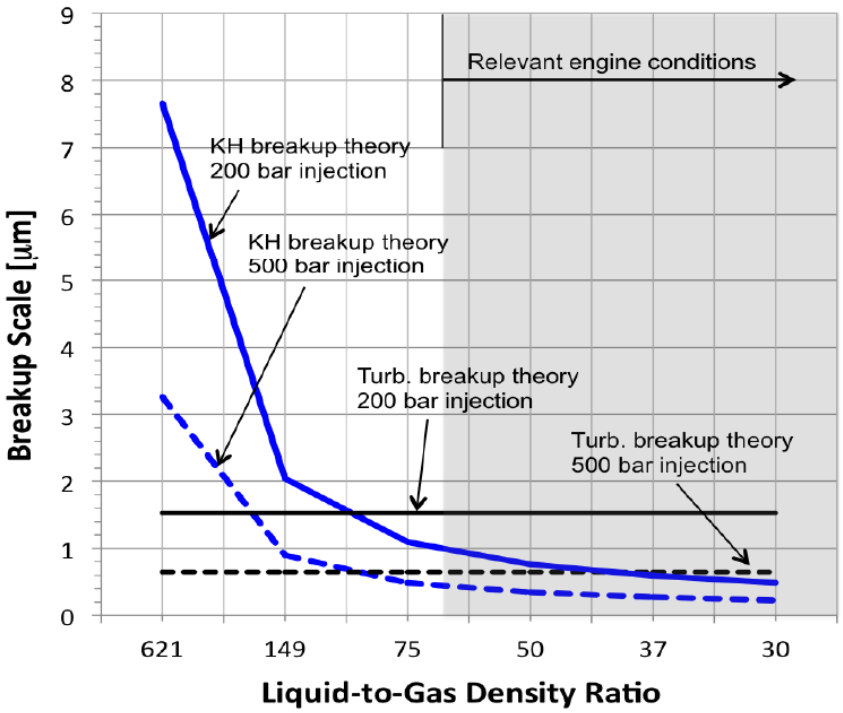

Figure 1 – Theoretical primary atomization scales as a function of liquid-to-gas density ratio

Reitz et al. and the model by Faeth et al. are shown in Figure 1. The figure shows a discrepancy between the two theories – that is if the liquid turbulence, or aerodynamic force, is the driving mechanism of the primary breakup, the breakup scale is insensitive, or sensitive, to the fuel-gas density ratio. To more accurately explain the discrepancy between the theories, researchers need to develop an imaging system with temporal and spatial resolution capabilities for direct visualization of in real fuel sprays, including high-pressure high-velocity liquid injections over a range of ambient density ratios.

2. Literature Review

1.2.1 Imaging system design

Direct visual validation of a primary atomization is difficult because of the small characteristic length scale (~1 μm) [6] and fast fluid speed (~620 m/s) in practical engine condition. To date, CFD models have been calibrated based on extrapolation of measurements at lower injection pressure conditions, far downstream measurements where spray imaging or other measurements are relatively feasible, or bulk characteristics such as a the jet spreading angle [11, 7, 8, 9, 10, 12]. Many types of imaging techniques have been utilized in an effort to capture an atomization event.

Typical light sources utilized for back-illumination imaging include the xenon arc lamp [8, 13], the laser [9, 10, 13], and the light emitting diode (LED) [14]. Xenon arc lamps can output broadband incoherent illumination in a short amount of time at a very high power. However, their repetition rates can be as low as one per 40 seconds [13], which makes it inapplicable for observing fast transient events. A pulsed laser outputs a short-pulsed, high-power, narrow range of coherent illumination with a relatively high repetition rate (~2 kHz) [15]. The drawback of using lasers in back-illumination imaging, is that their coherence contributes to constructive and destructive interference as the light passes through various mediums, which manifests as a random intensity distribution in the image, also known as a speckle pattern, as shown in Figure 2. Speckle is the interference pattern created by this optical path difference which is multitudes of constructive and destructive irradiance levels [16]. Speckle patterns are problematic because they add noise to images and make the speckle particle indistinguishable (Figure 2). Speckle patterns can be reduced

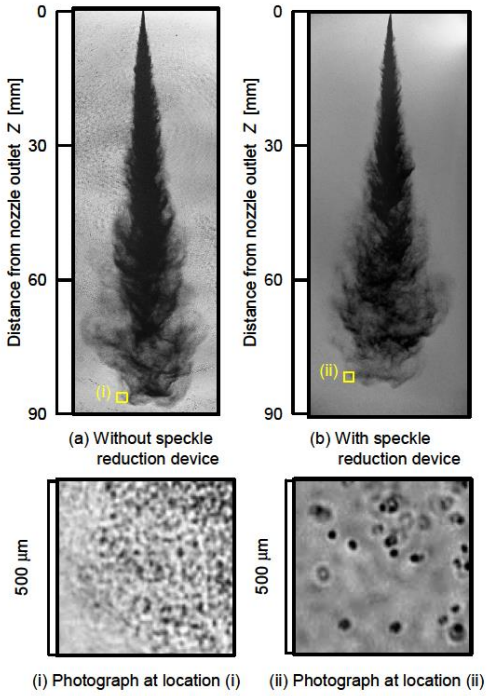

Figure 2 – Spray image with and without the speckle pattern, reproduced from [55]

by introducing a certain degree of incoherence into the beam path using a diffuser [17, 18, 19, 20]. Researchers have recently begun to use high power LEDs for back-illumination imaging, which combine the advantages of the two other light sources [14, 21]. LEDs produce short pulsed incoherent narrow band lights with a continuous high repetition rate and a relatively high power. For these reasons, LEDs allow for imaging at a high framerate without the addition of speckle noise to back-illuminated images.

1.2.2 Imaging experiments for high-pressure fuel sprays

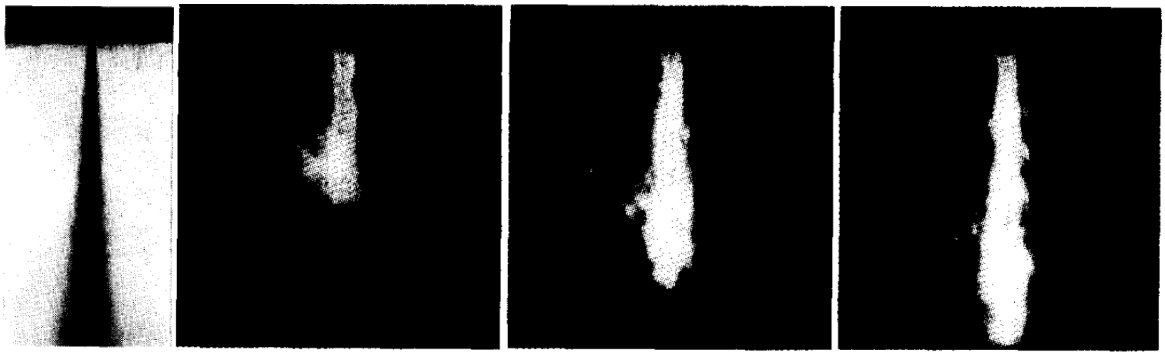

Figure 3 - Shadowgraph showing spreading angle and early penetration of liquid fuel spray, reproduced from [7]

The following researchers have contributed to visualizing the primary atomization. Reitz and Bracco are two of the earliest observers of automobile spray breakup. They have conducted numerous experiments to validate the theory of atomization for high pressure fuel sprays [7]. Images were obtained using high speed camera with 1.25 Mfps and two xenon flash tubes to shadowgraph the jet [7]. A framerate of 1.25 Mfps is an impressive achievement for their era but the resolution of images was limited (Figure 3). They could only measure the bulk quality such as a spread angle and jet length with lack of microscopic details.

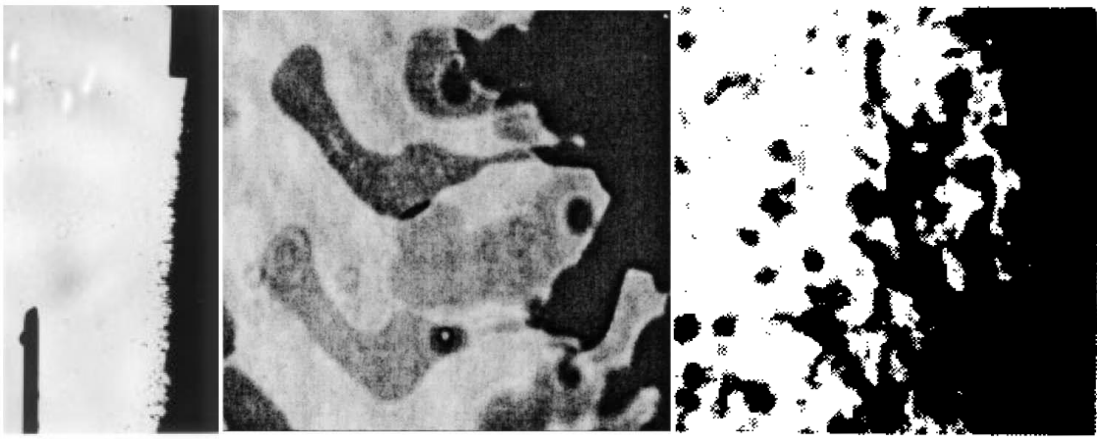

Figure 4 - Left: A pulsed shadowgraph at near nozzle, fluid speed = 28.2 m/s, reproduced from [10] . Center: a shadowgraph of a ligament base at surface of turbulent free jet, reproduced from [9]. Right: a hologram of water jet, reproduced from [12].

More recently, Faeth and his coworkers have used holography with shadowgraphy in an effort to visualize micro-details of jets such as ligaments and drops on turbid liquid surfaces [9, 10, 12]. Figure 4 demonstrates the clarity of image they could achieve. For the resolution, their imaging system allowed 5 μm objects to be detected and 10 μm objects to be measured with 10 % accuracy [9, 10]. Their images were clear but taken at a much higher liquid-to-gas density ratio (690 - 860) [9, 10, 12] where aerodynamics have less effect on the breakup process, while the engine relevant condition density ratio stands around 60.

As high-speed camera technology has advanced, the pixel resolution of images and the maximum framing rate has improved. Crua and coworkers have demonstrated long-range microscopy with an ultra-high-speed camera, long distance microscope, and long-single pulsed xenon flashgun [13]. Their camera had capability to image with a frame rate of 200 Mfps for 16 images, at 1280 x 960 pixels image resolution and 995 x 746 μm field of view. Crua and coworkers also demonstrated a speckle reduced laser for a high-resolution microscopy. This system had a 0.6 μm/pixel spatial resolution and a 768 x 614 μm field of view. The system was limited to a single image but with a high resolution. Images were taken at the beginning of injection in which the fuel speed is slower and the resolution of images was improved (Figure 5). Their work was focused on identification of residual fuel which is trapped after each end of injections.

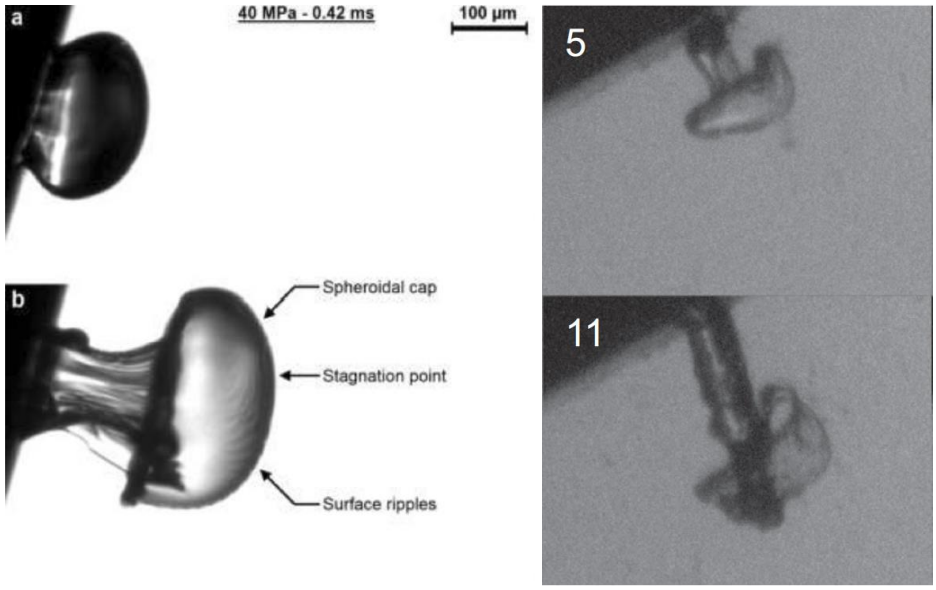

Figure 5 - Shadowgraph of an initial injection event imaged with Left: high-speed camera. Right: ultra-high-speed camera. Figures reproduced from [13].

Manin et al. have also demonstrated effective high speed microscopic imaging of diesel sprays [14]. They used a 200 ns pulse duration high repetition rate LED light source with a high-

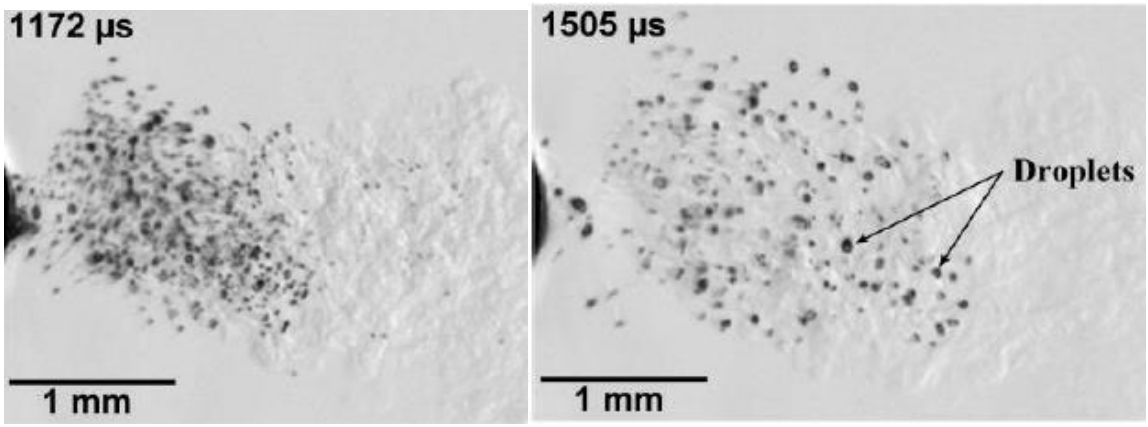

Figure 6 - Shadowgraph of fuel evaporation at end of injection, reproduced from [14]

speed camera (18 kfps). Images were taken at the end of the injection where the liquid speed is slower, yielding much clearer images (Figure 6).

Pickett et al., again from the Sandia National Lab, had a similar setup to that of Manin et al., to visualize the near nozzle fuel structure and the growth of diesel spray, using a high-speed

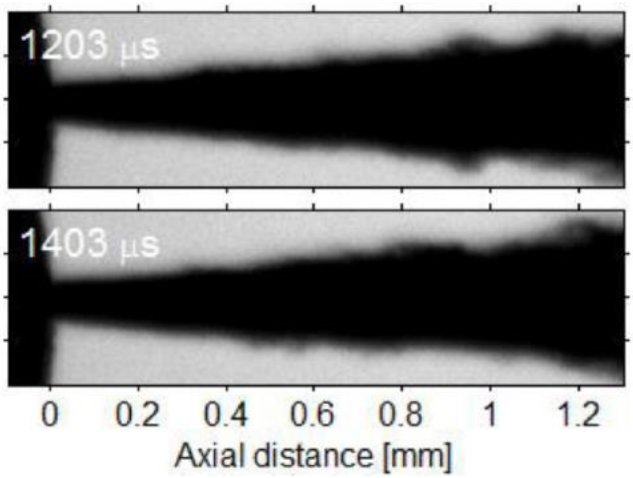

Figure 7 - Optical spray microscopy visualization with diffused backlighting. Microscopic structures are not discernable. Figures reproduced from [21]

LED pulsed at 50 ns (Figure 7) [21]. Their spatial resolution was 4.7 µm/pix, field of view of about

1.4 mm in a 320x96 pixel region of interest, and 156 kfps frame rate [21]. Their image did not show droplets or ligaments during the injection because the fuel was traveling at too fast speed within the optically dense region. However, the droplets and ligaments were observable at the end of the injection [21].

Figure 8 summarizes the primary breakup regimes over which each of the prior experiments were conducted. Crua and coworkers' work [13] is not included because their work is not near atomization regime. Reitz and Bracco's [7, 22] work was near gasoline engine condition but their images suffered from low resolution. Pickett and Manin from Sandia National Lab [14, 21] were diesel engine relevant condition but their images were either taken at the end of injection or they also suffered from lack of microscopic details. Faeth and coworkers' experiments [9, 10, 12] were done at 2nd wind induced breakup mode which is not engine relevant condition.

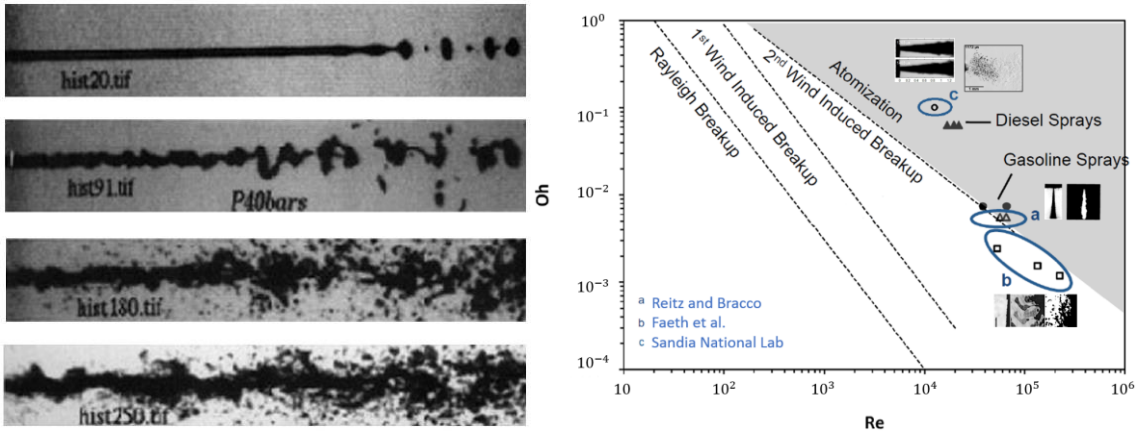

Figure 8 - Left: Typical pictures of jet breakup, categorized by regime, from top to bottom: Rayleigh, first wind-induced, second wind-induced, and atomization. Figure reproduced from [54]. Right: Regime locations for sprays investigated in literature, breakup mode limites categorized by Reitz. Figure reproduced from [22].

1.2.3 Objectives of the thesis

Reitz and Bracco was able to achieve high frame rate but a low resolution. Faeth and coworkers imaging system had a high resolution but their system was limited to single images. Crua and coworkers had two separate systems – one that achieves a high frame rate but with a relatively low resolution, and one that achieves a high resolution but with a single frame image. Manin and coworkers used an imaging system with a medium frame rate and high resolution. Finally, Pickett and coworkers used an imaging system with a high frame rate but low resolution. The common difficulty that the previous researchers encountered was capturing both the high frame rate and resolution. In this thesis, a new imaging system with the combination of the following advantages will be discovered:

- High frame rate, comparable to Crua and coworkers' ultra-high-speed camera [13]
- High optical resolution, comparable to Faeth and coworkers' high resolution images [9, 10]
- High FOV, comparable to Crua and coworkers' high resolution images [13]

The new diagnostic imaging system is aimed to enable a direct imaging of primary atomization of fuel injection at an engine relevant condition.

TECHNICAL APPROACH AND EXPERIMENTAL SETUP

3. Concept of Spectral Microscopy

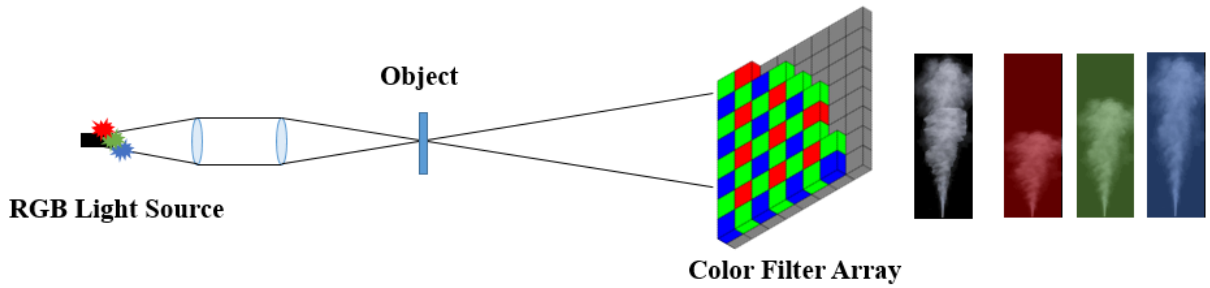

Figure 9 – Schematic representation of spectral imaging. The frame rate and shutter duration is controlled by light sources.

High speed cameras are limited by a maximum number of read-out pixels per second, which limits the maximum framing rate and image size. In other words, a faster framing rate requires a smaller image size or number of pixels. A new high-speed imaging technique is proposed called spectral microscopy, which overcomes this drawback by utilizing an image sensor color filter array (CFA) and 3 individual colored light sources. The idea is described schematically in Figure 9. Color camera sensors are coated by a thin layer of color filters. Colors of the filter are commonly the three additive primary colors: red, green, and blue (RGB) [23]. Each pixel in the sensor area is coated with a different color filter, creating a fixed pattern of red, green, and blue pixels. With a sufficiently long camera shutter duration, color light sources with wavelengths that overlap with the detection bandwidth for each of these color filters can pulse at a different time consecutively within a single imaging event. The single acquired image will then contain three temporally distinct monochrome color images of the subject (e.g. red, green, and blue), which can be separated via post-processing. Ultimately, the exposure time is determined by the pulse width

and pulse separation of the color light sources, and the frame rate is determined by the time between pulses. The main advantage is that the image size is always at the maximum regardless of the frame rate, unlike the conventional high-speed camera.

4. Back Illumination Imaging Setup

1.4.1 Approach to select illumination source and wavelength

Quantum efficiency is the ratio of incident photons to converted electrons of photo-sensitive devices. Closely related, spectral sensitivity is a sensitivity of the photo sensor to optical radiation of different wavelengths [24]. The spectral sensitivity of the camera sensor needs to be well understood to select appropriate illumination colors for effective spectral microscopy images. A RGB CFA has three band-pass filters, with each filter demonstrating a peak transmission near red, green, and blue wavelengths and have overlaps each other (Figure 10). For instance, yellow

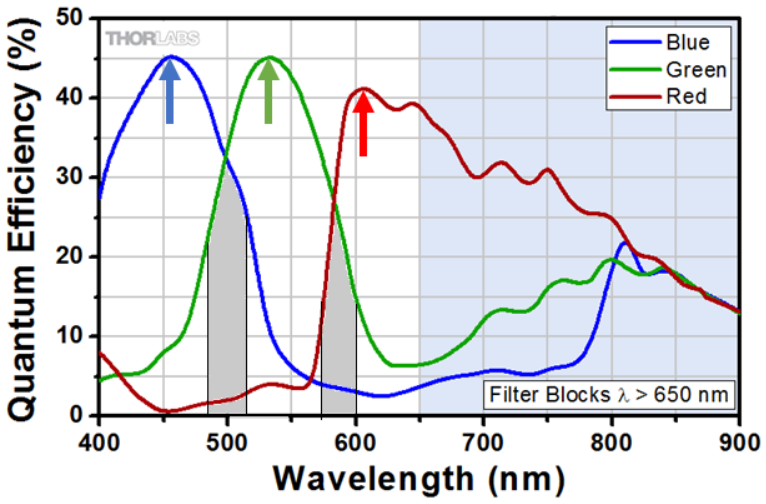

Figure 10 – Example quantum efficiency plot of a Thorlabs camera DCC1240C. Grey shaded areas are vulnerable to the color crosstalk.

light near 500 nm can transmit through both red and green color pixels because of their wavelength overlap on the color filter. This is called color crosstalk and should be avoided to obtain three distinctive images. To explain the color crosstalk, is a CMOS quantum efficiency of a Thorlabs camera is shown in Figure 10. Using wavelengths within the grey shaded area of Figure 10 can introduce the color crosstalk, while using wavelengths at peak quantum efficiency guarantees the highest contrast in images. In this case of Thorlabs camera, light sources with wavelengths 450 nm, 550 nm, and 650 nm should be used to both avoid the color cross talk and maximize the contrast in images.

For the spectral microscopy system developed in this thesis, a DSLR camera Nikon D5300 was used. Nikon does not provide sensor-specific quantum efficiency or spectral sensitivity plot, so it was directly measured. Sigernes et al. [25] measures an absolute quantum efficiency of a digital camera, and their experimental setup is modified to measure our camera spectral sensitivity (Figure 11). The wavelength of the monochromator was swept from 350 nm to 700 nm with an increment of 10 nm. The light from the monochromator was shot into the integrating sphere, which re-directed the light into the microscopic lens and the camera assembly. The ISO setting for the camera was set to be the lowest (100) to minimize the noise amplification. The shutter speed was set to 3 seconds, to receive the enough light and avoid the oversaturation. Images were taken with the Nikon proprietary .NEF format, which was then converted into a more universal .tiff format. The converted .tiff images were then directly read as 3-layer 2D matrices. The first, second, and third layer corresponds to data red from the red, green, and blue filtered pixels, l respectively. A dark frame was subtracted from each image to remove thermal noise. The intensity of each image was then averaged over the field of view and multiple images were recorded over the range of wavelengths swept by the monochromator. The focus of this exercise was to determine the

wavelengths of peak detection for each color filter on the camera sensor and the magnitude of filter overlap at specific wavelengths, so calibration of the optical power was not performed.

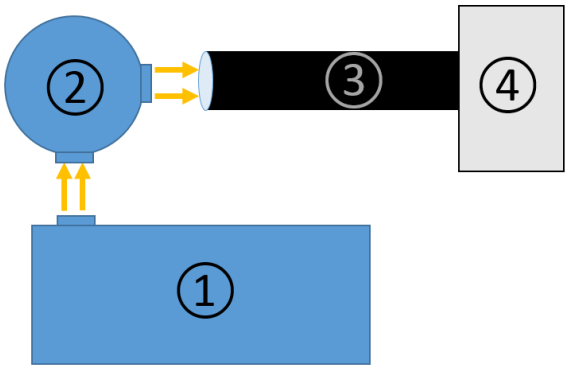

Figure 11 – Spectral sensitivity measurement setup has, ① a Perkin-Elmer 650S fluorescence detector with monochromator, ② a Newport 819C-SF-4 integrating sphere, ③ a long-distance microscope, and ④ a Nikon D5300 DSLR camera

1.4.2 Approach for Design of the Optical System

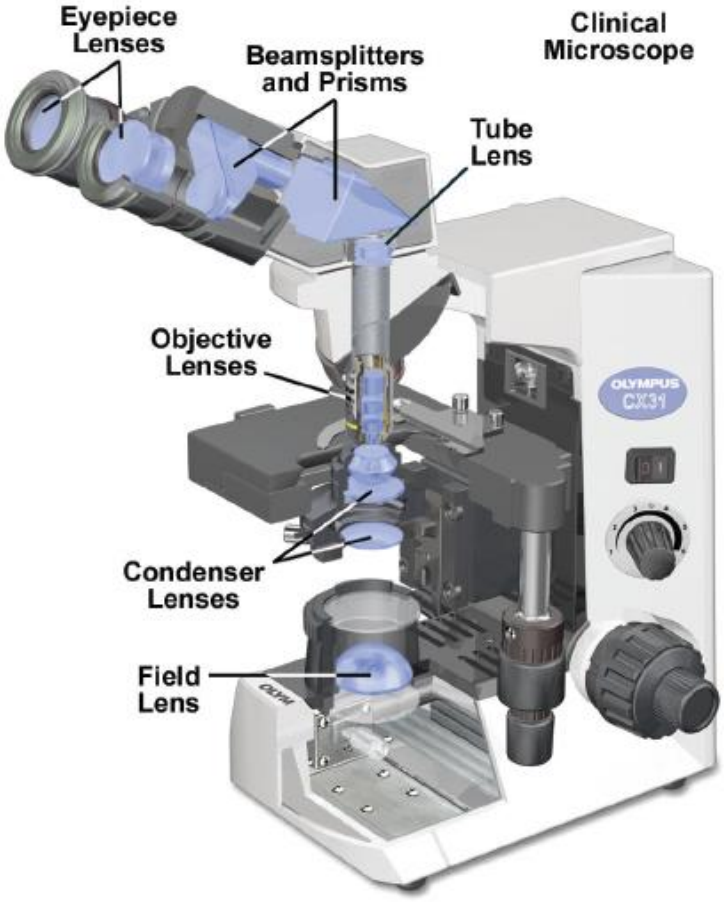

Figure 12 - Diagram of a typical modern microscope. A specimen is placed between an objective lens and a condenser lens. Diagram reproduced from [29].

The optical train design for the spectral microscopy system developed in this thesis followed several basic microscope design principles. Figure 12 is a diagram of a typical modern microscope with labeled parts, showing that the specimen, or a target, is placed between a field condenser and an objective. Equation (1) through (3) are some basic properties of the lenses and relationship between one another. n is the refractive index, α is half of the angular aperture, f is the focal length, and D is the diameter. Angular aperture is defined as the angular difference

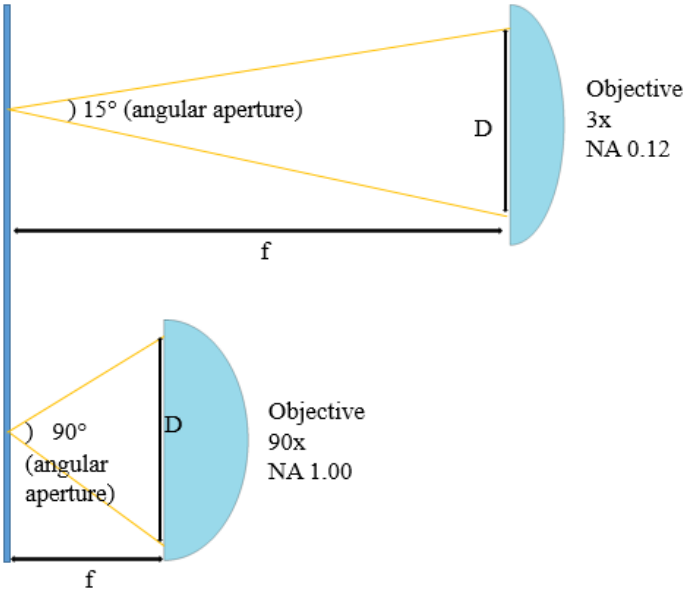

Figure 13 - General relationship among NA, magnification, and light collection angle

$$Numerical\ Aperture\ (NA) = n\ sin\alpha \tag{1}$$

$$f - number\ (f\#) = \frac{f}{D} \tag{2}$$

$$f\# = \frac{1}{2NA}\ , using\ small\ angle\ approximation \tag{3}$$

between the paths of the most divergent rays, which any lens can thus gather up and bring to a focus [26]. Figure 13 shows a diagram of these basic terminologies for geometrical optics and demonstrates that an increase in the angular aperture also increases the NA, and generally increase the magnification. With the terms and equations, the properties of condenser and the collimating lens are defined.

A field condenser focuses the incoming light to illuminate the target or species. However, illumination is not the only role of the field condenser. To understand how a field condenser can

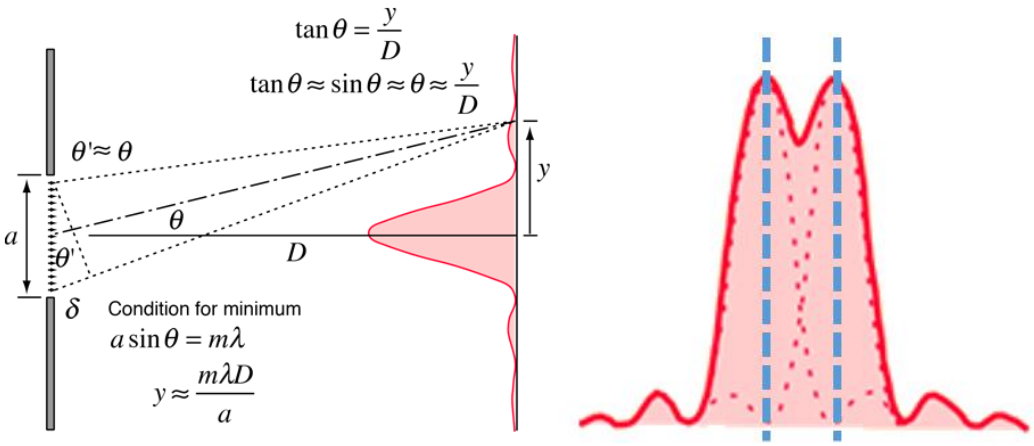

Figure 14 – Left: Single slit diffraction diagram, reproduced from [58] and Right: resolved image of two slits

affect the overall resolution of an image, definition of the resolution needs to be addressed. For diffraction-limited optics, Ernst Abbe was the first to quantify the resolving power [27]. This resolving power is nowadays typically called the "Abbe resolution." For objects on the order of the wavelength of the illuminated light, the resolution is directly related to the diffraction interference pattern created by an object. Figure 14 is a simple representation of a single slit interference and equation (4) is the condition of a destructive interference pattern [28]. The 1st order destructive interference Equation (5) can be derived by replacing the D/a with the definition

$$y = \frac{m\lambda D}{a} \tag{4}$$

$$y = \frac{\lambda}{2NA} \tag{5}$$

$$y = \frac{\lambda}{NA_{condenser} + NA_{objective}} \tag{6}$$

$$y = \frac{1.22\lambda}{NA_{condenser} + NA_{objective}} \tag{7}$$

of the NA from equation (3). This is also known as Abbe criterion and it finds the smallest object that can be resolved with the wavelength and NA of the lens. The Equation (6) is an expression of Abbe criterion that is widely used in microscopical society when the NA of the condenser and objective lens are not exactly the same [29]. Abbe criterion is for two slits which are placed close together, and that second slit's zeroth order maxima is placed at the first slit's first minima. The equation (7) is for circular pattern object and is called Rayleigh criterion.

To verify that the image with and NA matched condenser produces better resolution than collimated light, a resolution comparison was made with and without a NA matched field condenser. The resolution was measured and quantified with the modulation transfer function (MTF), which is presented in Section 1.5.2. The justification of green wavelength will be mentioned in the 1.8.1 Spectral Sensitivity Result. Figure 15 is the experimental setup for

resolution comparison. Both setups will have identical optical properties, except the presence of a NA matched field condenser.

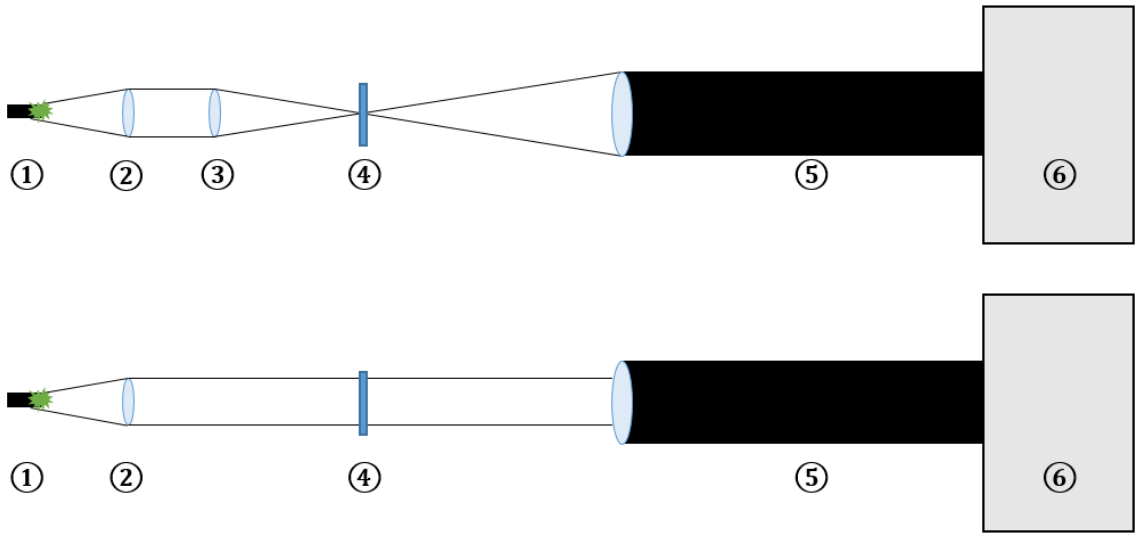

Figure 15 – Experiment setup to quntifying effectiveness of the NA matched field condenser includes, ① continuous green LED light source, ② collimating lens D=50 mm, f=32 mm, ③ field condenser lens with effective Diameter = 50 mm, f=12.5 in, ④ USAF resolution target, ⑤ long distance microscope NA=0.083, ⑥ Nikon D5300

The collimating lens controls the spot size at the imaging plane and the contrast of images. The spot size can be defined by optical invariant, and the resulting contrast can be found with the similar setup as described in upper setup of Figure 15. The result of the spot size calculation and the contrast comparison will be made in section 1.8.2.2.

5. Approaches for Quantifying the Spectral Microscopy Image Resolution

Modulation transfer function (MTF) is a direct and quantitative measure of the image quality [30]. When discussing an imaging system, it is sometimes not easy to say which image has the better resolution purely by visual inspections, but quantification is needed to scientifically

evaluate the imaging system. In section 1.4.2, a method of finding the theoretical resolution of an optical system has been investigated. However, the theoretical diffraction-limited resolution is never achieved because of imperfections of optical system components. Measuring the MTF of a system can quantify the achieved resolution by estimating the fineness of the detail that an imaging system can resolve.

1.5.1 Measuring Image Blur with the Modulation

A modulation function, such as a sine wave, can be used to measure image blur caused by diffraction and other imaging system aberrations. A 1951 USAF resolution test target (Figure 16) contains a standardized set of bar patterns that can be used to measure modulation. Notice that as the bar patterns get smaller, the more difficult it becomes to recognize the black bars between the white bars. Figure 17 demonstrates this phenomenon more directly by showing schematically how the bar pattern image looks and its corresponding modulation [31]. The modulation [32] transferred to the image, or sometimes referred as the image contrast, is a parameter which evaluates the performance of imaging system and it is calculated with equation (8). The ratio of image modulation and object modulation (equation (9)) is the contrast transfer function (CTF), which is similar to the MTF but not used in this work. When the modulation reaches zero, the line grating image looks completely grey and the pattern is not recognizable anymore (Figure 17).

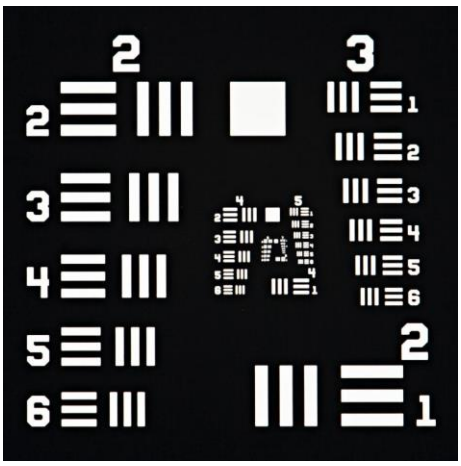

Figure 16 –1951 USAF resolution test target.

$$Modulation = \frac{I_{max} - I_{min}}{I_{max} + I_{min}} \quad (8)$$

$$CTF_i = \frac{\text{Image Modulation}_\text{i}}{\text{Object Modulation}} \quad (9)$$

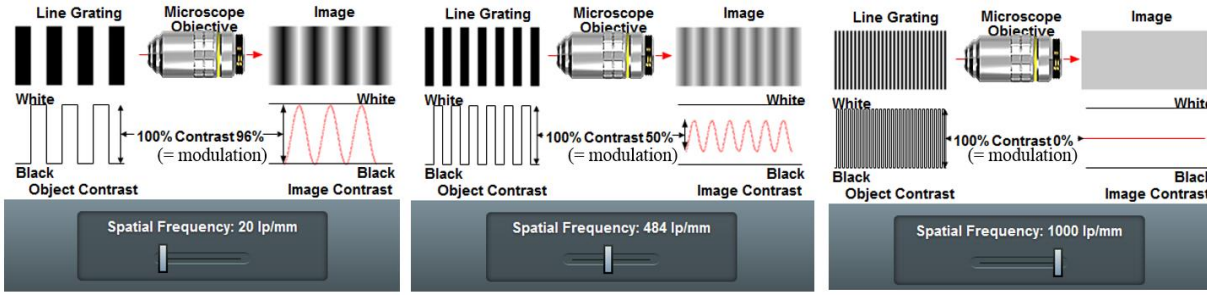

Figure 17 – The modulation of an imaging system decreases as the line grating spatial frequency increases, reproduced from [31]

1.5.2 Measuring resolution with the Modulation Transfer Function (MTF)

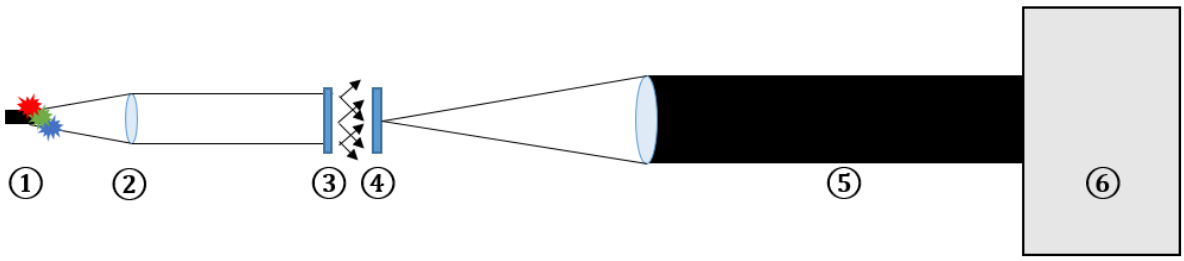

Figure 18 – Experimental setup for MTF measurement includes, ① LED light source with wavelengths of 627 nm, 530 nm, and 447.5 nm, ② collimating lens D=50 mm, f=50 mm, ③ diffuser, ④ 1951 USAF resolution target as a slanted knife-edge placed at a focal plane, ⑤ long-distance microscope NA=0.083, and ⑥ Nikon D5300.

MTF is considered as the standard for measuring the resolution of an imaging system [33]. The MTF measures the resolution by imaging a tilted knife edge. The ISO 12233 provides a standardized code to measure the MTF of an imaging system from an image of a tilted knife edge [33]. Figure 18 describes the overall experimental setup for the MTF measurement. The

justification for the wavelengths of light sources is in section 1.8.1. A diffuser was placed before the target, according to the ISO 12233 section “Visual resolution measurement” [33]. Putting a Lambertian diffuser behind the target serves two purposes: 1) It provides a uniform illumination in testing section, 2) It simulates a field condenser with a high NA and thus enables the objective to fully utilize its NA, same mechanism as section 1.4.2. The shutter duration for the camera was chosen so that images were illuminated to near full scale of the sensor’s full well capacity (2^{14} bit), but not oversaturated. A 1951 USAF resolution test target was placed at each wavelengths’ own focal plane. Each wavelengths’ focal plane was found with frequency domain image quality method which is discussed in 1.6.3 Longitudinal Chromatic Aberration. The camera ISO sensitivity is set to the minimum (100) and the continuous light was used. The MTF is independent of the contrast [34], but more photons help increasing the SNR. Note that the ISO 12233 calls MTF as the edge-based spatial frequency response (e-SFR), and it provides the ISO 12233 e-SFR code [33]. The basic logistics behind the e-SFR code is as follows. Once the knife edge is imaged onto the sensor as described in Figure 20, the angle of the slanted edge is measured and the oversampling rate is calculated using the Equation (10). Oversampling rate defines the number of pixel rows that the knife edge covers from the dark to the bright. Pictorially, the gradation of the knife edge covers exactly from pixel e2 to pixel e9 in Figure 20, making the oversampling rate of 8 at an angle of approximately 97°. This oversampling rate defines the size of “pixel considered.” Each pixel column is then projected to a single row to make a gradient of intensity (Figure 20) [35, 36]. The intensity of the projection row forms an edge spread function (ESF). The derivative of an ESF is a line spread function (LSF). Acquired LSF contains noise, so use the Hamming window on the LSF to reduce the noise. Finally, the discrete Fourier transform function of the LSF is an MTF. Figure 19 is a simplified depiction of deriving process of an MTF. The resolution of an

imaging system is defined by the spatial frequency (cyc/mm) in which the modulation reaches 50% for the reasonable image quality [34], 10% for the near limit [33], 0% for the absolute limit [37]. ISO uses 10% as the resolution limit, so the plots in this paper will only show down to 0.1 of MTFs.

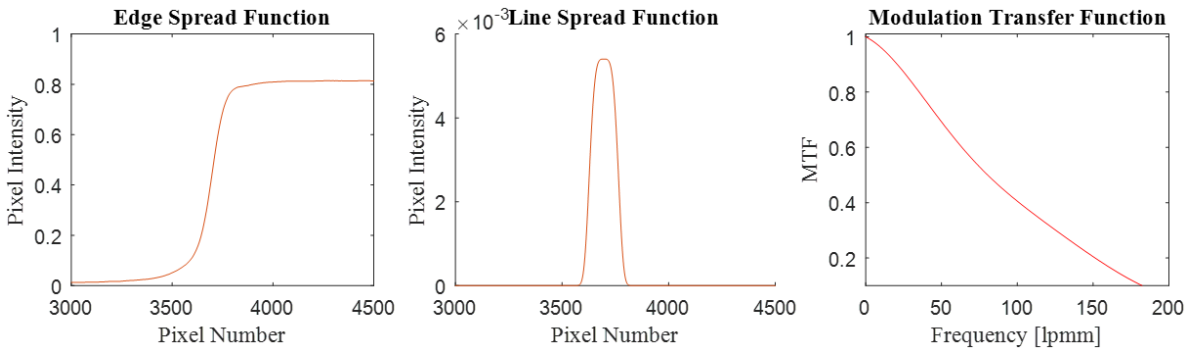

Figure 19 – Example process of MTF calculation.

$$oversampling\ rate = abs|tan\theta| \tag{10}$$

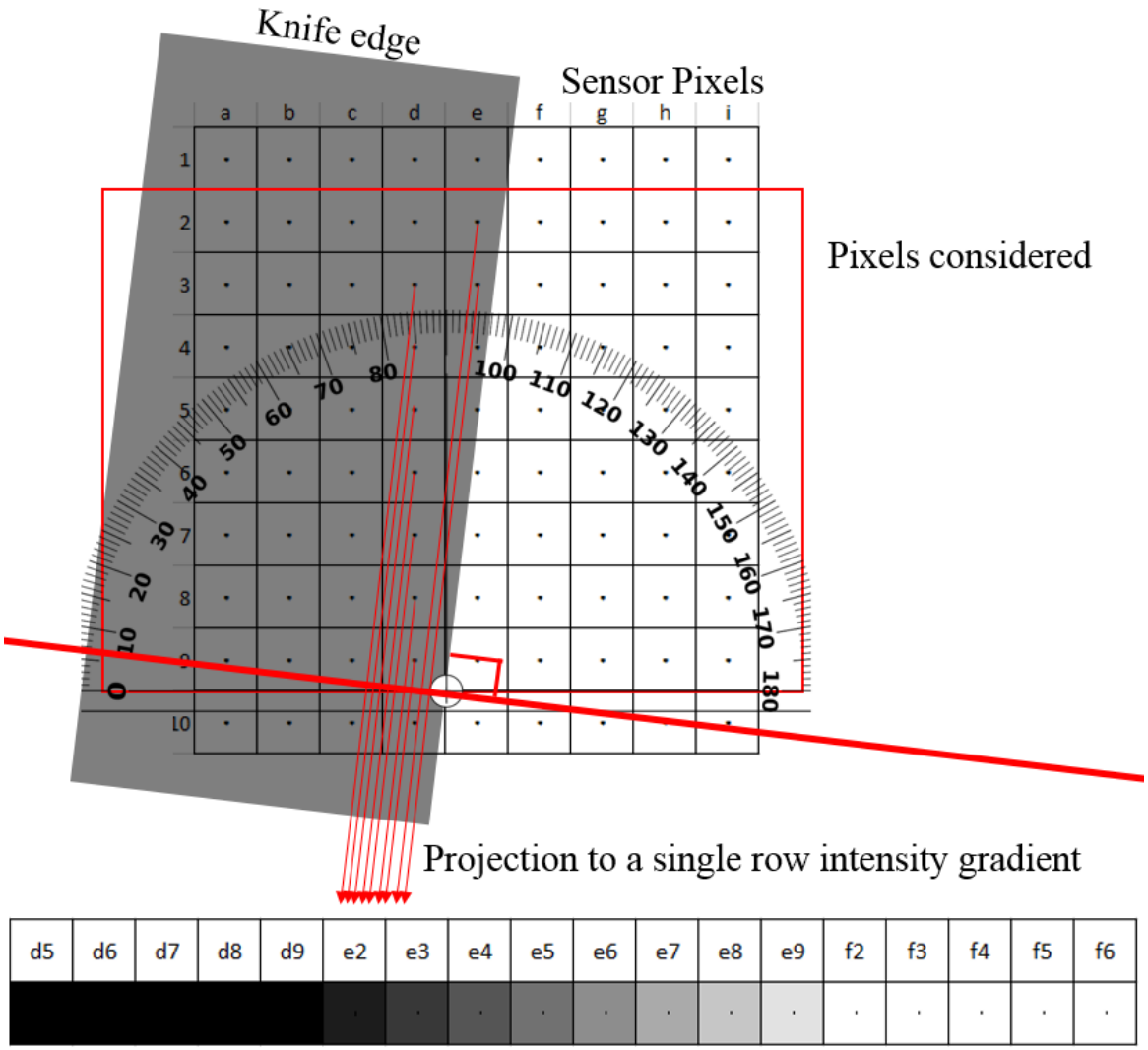

Figure 20 - Slanted Knife Edge logistics. A slanted knife edge creates a row of an intensity gradient, which is used for the MTF analysis.

6. Quantifying Effects of Multi-Color Digital Imaging on Image Quality

1.6.1 Configuring Color Filter Array Pattern

The resolution limit of an imaging system is not only dependent on optical resolution as discussed in the section 1.4.2, but also dependent on the spatial resolution of the digital camera sensor. According to the Nyquist theorem, the spatial resolution is two times of the pixel pitch [38]. The Equation (11) calculates the sensor resolution with a given pixel pitch. For example, if the pixel size is 10 µm x 10 µm; there's no gap between the pixels; magnification of 1; the spatial resolution becomes 50 cyc/mm. The pixel pitch can be found from a manufacturer spec sheet, but

$$Nyquist\ limited\ spatial\ resolution\ [lpmm] = \frac{Magnification}{2 * pixel\ pitch\ [mm]} \qquad (11)$$

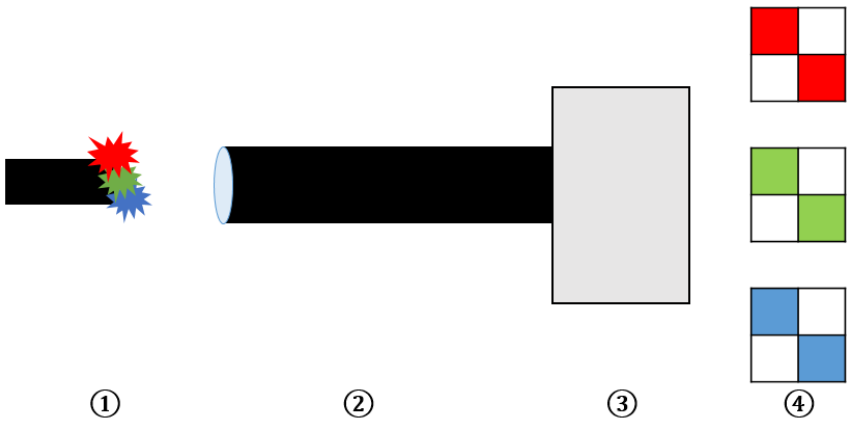

Figure 21 – Experiment setup for finding the CFA includes, ① Light source wavelength 627 nm, 530 nm, and 447.5 nm, ② Microscopic lens, ③ Nikon D5300, ④ Expected CFA pattern.

the type of color filter array for color cameras is not usually listed. While the Bayer pattern is the most common form of the CFA, there are various forms of the CFA and each form has their own characteristic spatial resolution. Finding this array pattern is also important when de-mosaicing,

which will be discussed in the section 1.6.2. The pattern can be found by directly imaging a single wavelength light source. Figure 21 is an experimental setup for finding the CFA of the camera. Dim light sources with three wavelengths 627 nm, 530 nm, and 447.5 nm are imaged at the corner of the camera. The justification of three wavelengths are discussed in the 1.8.1. DNG method of the de-mosaic algorithm, which is explained in the section 1.6.2, was used to show the mosaic pattern of the CFA.

1.6.2 Color Filter Array De-mosaic

Nikon cameras takes lossless images in the .nef format. This lossless format needs to be converted into .tif format to be able to read. Eddins introduces a conversion method which can read .nef image as a mosaic pattern of a color filter array as shown in Figure 22 [39, 40]. This method guarantees the closest to the raw image and will be used for reading all the images in this paper. To convert a .nef raw image file to a .tiff mosaic pattern, the .nef file is first converted to an Adobe raw file format .dng. From there, the MATLAB can convert a .dng to a .tiff with its

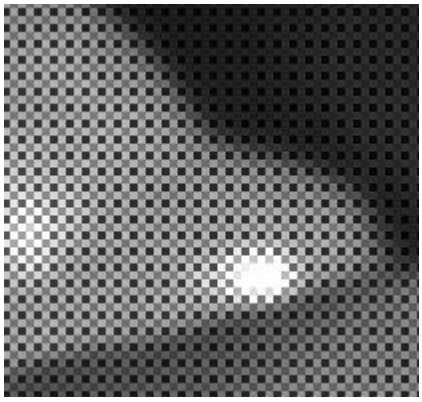

Figure 22 – Mosaic pattern of a color filter array on an image, reproduced from [39]

built-in function [40]. For Nikon cameras, the images then need to be linearized because Nikon applies a non-linear transformation for storage purposes [39]. At this point, the image is a 2D matrix of CFA mosaic pattern as shown in Figure 22 and the CFA array pattern can be found. For a typical Bayer filter, there are 4 variations of patterns depending on what order the RGB colors are aligned: gbrg, grbg, bggr, and rggb. The MATLAB provides a built-in de-mosaic algorithm depending on the CFA pattern, in which it interpolates pixels and make three layers of RGB images.

1.6.3 Approach for Defining the Longitudinal Chromatic Aberration (LCA)

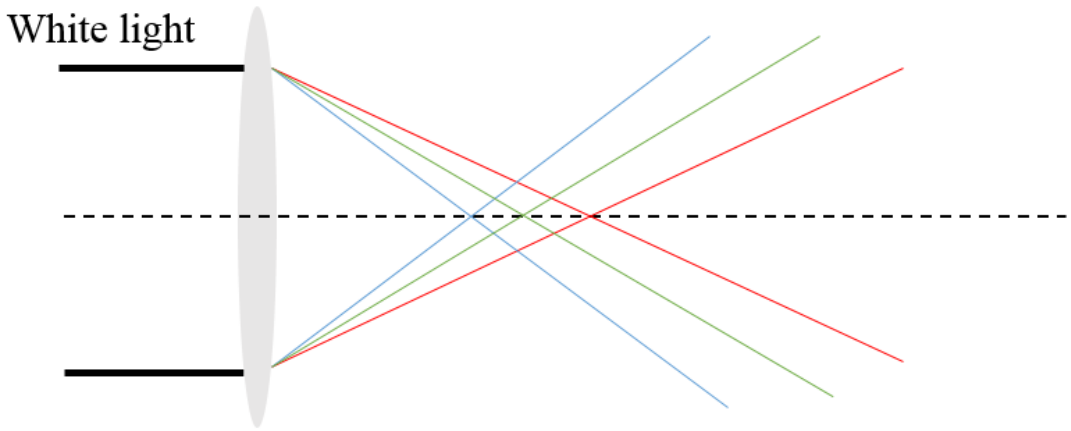

Figure 23 – Longitudinal Chromatic Aberration. RGB colors have different focal plane because of the refractive index dependency on wavelength.

Longitudinal chromatic aberration (LCA) is an image blur caused by the refractive index dependency on the wavelength. Typically, the refractive index increases with decrease in the wavelength and this causes the lens focal length in the blue light to be shorter than focal length in the red light. The Figure 23 depicts this RGB light being separated from the white light and focused

at a different location. Hecht describes this phenomenon as the periphery of the image being tinged

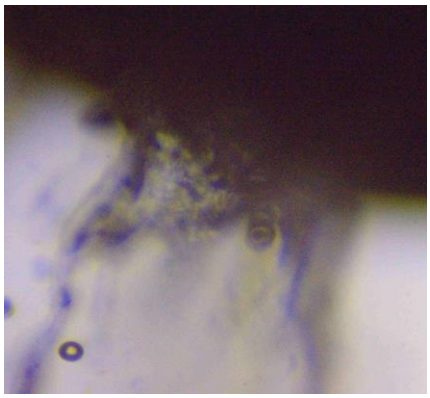

Figure 24 – Demonstration of the chromatic aberration in a water jet image. Yellow and blue tints are visible around the blurred figure

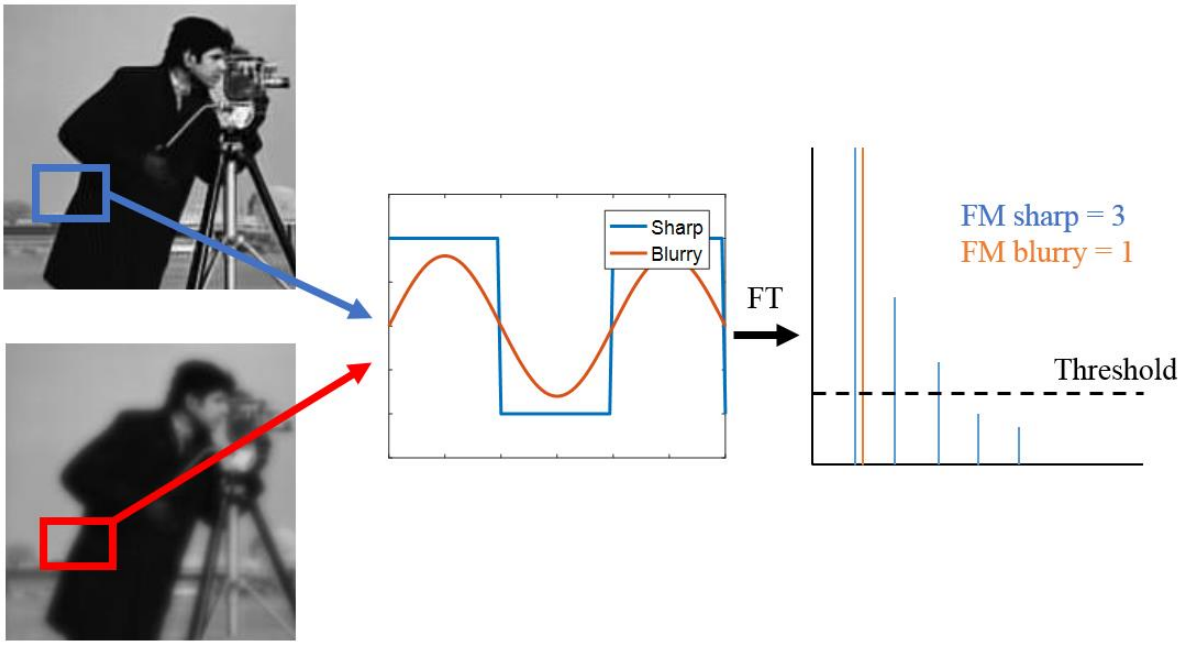

Figure 25 – Logistics of the FM, the method suggested by De et al. [41]. Sharp images have higher number of FM than blurry images.

in orange-red or blue-violet depending on the object location [32]. This description was visible in one of the early stage images of water spray (Figure 24). If LCA is larger than the depth of field

$$LCA = WD_{max} - WD_{min} \quad (12)$$

(DOF) of the microscope, it means images with a different color will be blurry because of the image plane being out of focus. To measure the LCA, the location of focal planes for each RGB must be found. Focal planes can be found by measuring the working distance (WD) when the image is in focus. The WD is a distance from the focal plane to the objective lens. To be able to discern that the image is in focus, two following methods can be used: measuring modulation, and measuring frequency domain image blur measure (FM) [41]. The FM is a no-reference image quality assessment in which it removes cumbersome necessity of the locating a knife edge or

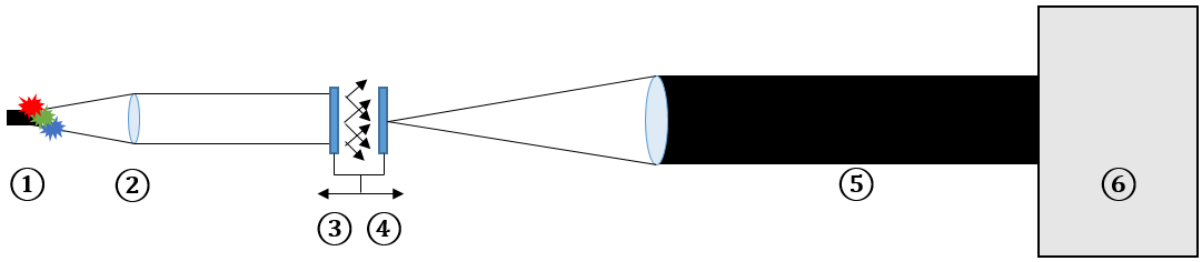

Figure 26 – Experimental setup for measuring the LCA includes, ① continuous LED light source with wavelength 627 nm, 530 nm, 447.5 nm, ② collimating lens D=32 mm, f=50 mm, ③ diffuser, ④ 1951 USAF resolution target placed at focal plane, ⑤ long distance microscope NA=0.083, ⑥ Nikon D5300.

frequency bar patterns in each picture [41]. The overall logistics is as described in Figure 25. Sharp image edges are closer to a step function while blurry image edges are closer to a sine wave with lesser amplitude. This is a similar analogy of Figure 17. A Fourier transform of a square wave and a sine wave is described in the rightmost image of Figure 25. The FM is a count of values that exceeded the preset threshold. Higher FM can be interpreted as sharp edged images and better focused images. Figure 26 is the overall experimental setup for measuring the LCA. ISO sensitivity for the camera is set to be the lowest (100). The diffuser and the resolution target are placed on a

same linear translation stage so that they can move back and forth as a single body while keeping the gap between them constant. First, method of finding the WD with the FM was validated by comparing the result with the bar pattern modulation. Modulation of a bar pattern will peak when the image is in focus, or the resolution target is at the focal plane. The modulation will reduce when the image is blurry, or as the resolution test target moves away from the focal plane. Images were taken with the 530 nm light at an increment of 1mm, and both FM and modulation were measured and compared. Second, to find WD of all three colors, images were taken with the RGB light at an increment of 100 µm. The FM was plotted against the WD, and the LCA was calculated with equation (12). In the Equation (12), WD_{max} is typically the WD with the blue illumination, and WD_{min} is typically the WD with the red illumination.

1.6.4 Defining the Size Error Caused by LCA

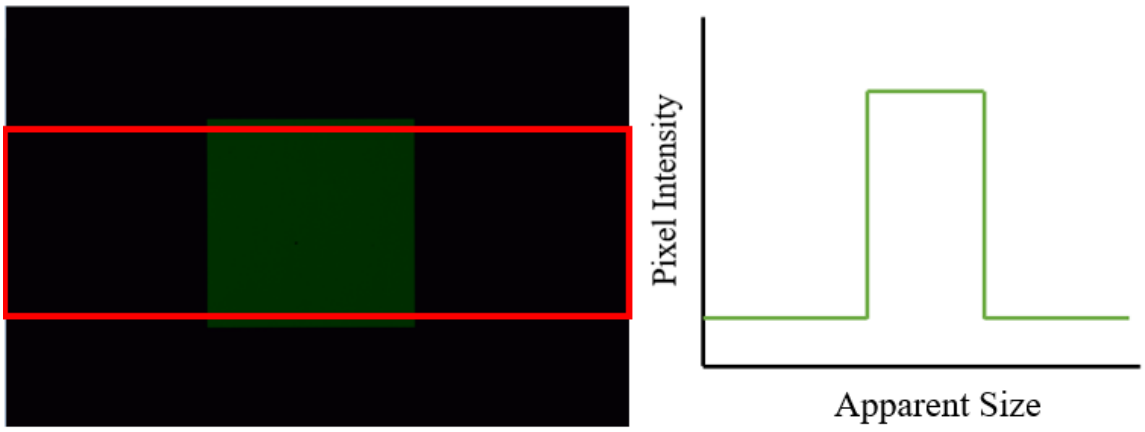

Figure 27 – Square target with a width 2227 µm is imaged and cropped to measure the FWHM

When the camera images a spray, droplets that are out of focus will appear as a different size from their true sizes. More specifically for a single beam illumination, the objects appear to decrease in size with increase in distance from focal plane [42]. Combining this with the LCA, where there are three distanced focal planes, a single droplet may appear as three different sizes depending on the illumination wavelength. For example, a droplet in the blue focal plane may appear bigger in green and the biggest in red. To study the effect of defocusing on the object size, the same experimental setup as measuring the LCA, Figure 26, was used. ISO sensitivity was set to 100, a steady state light was illuminating the target, and shutter duration was 1/4000 sec. A square on the resolution test target with the true size 2227 μm, which is the equivalent size of Group 0 Element 2 on the 1951 USAF resolution test target, was imaged at every increment of 200 μm. The horizontal section was cropped and averaged by columns (Figure 27). The full width half max (FWHM) was measured to determine the apparent object size.

7. Experimental Setup of Spectral Microscopy Imaging System

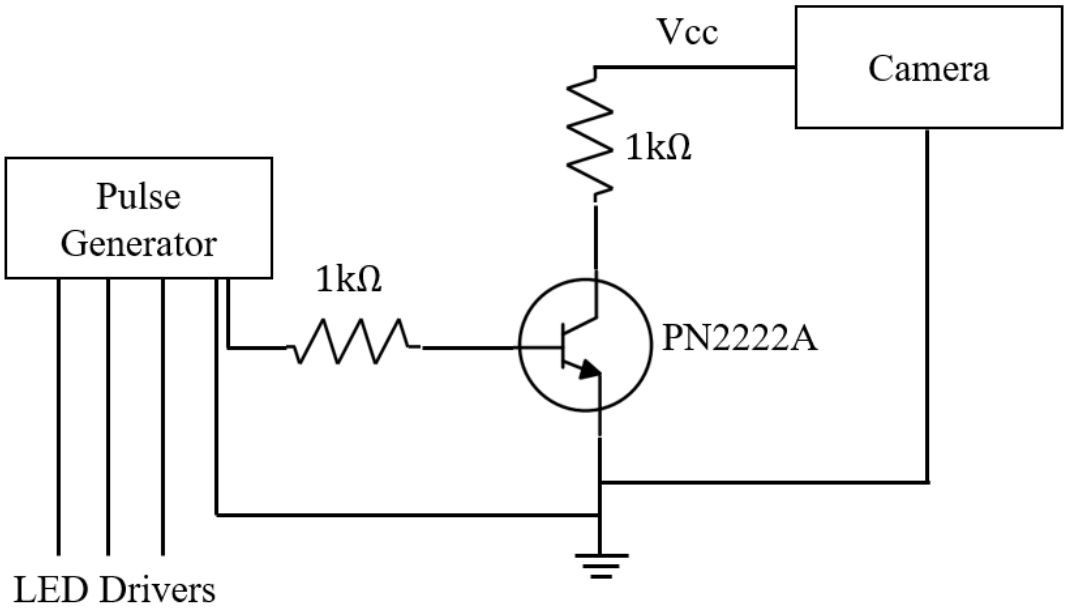

Figure 28 – Simple circuit for synchronizing a DSLR camera, pulse generator (BNC 577), and LED drivers

The camera shutter was synchronized with the LED drivers, so that the LED light pulses during the camera mechanical shutter is open. Figure 28 is the circuit for synchronizing the camera and LED drivers, with a pulse generator. The pulse generator sends out a TTL signal to the camera and waits approximately 1 sec before sending pulse signals to LED drivers. This wait is for the "exposure delay mode" of the camera, which the camera delays the shutter release for about 1 second to prevent the vibrational motion blur caused by the DSLR camera's internal mirror. The Nikon D5300 camera has a mechanical rolling shutter and the shutter duration of the camera needs to be long enough to avoid the partial exposure effect (Figure 29). For this reason, the shutter duration is set to a long 10 µs. For the light pulses, a short light pulse duration is critical for reducing the motion blur of the object. The LED pulse duration may be longer than what is commanded by the pulse generator, because of the delay within the LED driver circuit. To find

actual pulse durations, an experimental setup in Figure 30 was used. The pulse generator sends out a 10 ns pulse to the LED driver. A photodetector was connected to an oscilloscope to measure the FWHM of the light pulse.

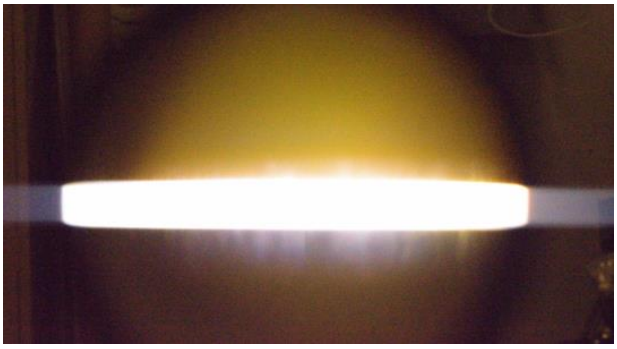

Figure 29 – Image of flashing light with a rolling shutter. High shutter speed caused partial exposure.

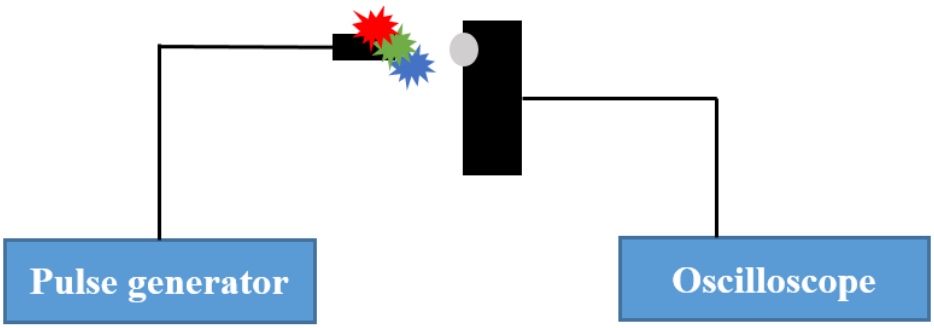

Figure 30 – Experimental setup for verifying the pulse width of LED drivers. An oscilloscope is connected to a photodetector (Thorlabs DET10).

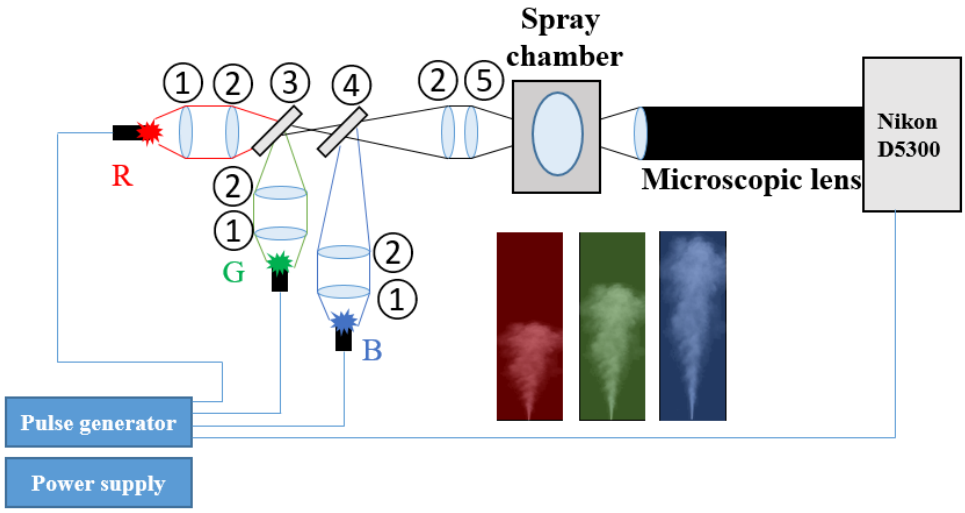

Figure 31 – Overall experimental setup includes, ① collimating lens (f=32 mm, D=50 mm), ② matching lenses (f=125 mm, D=50.8 mm), ③ long pass dichroic mirror (605 nm), ④ long pass dichroic mirror (505 nm), ⑤ field condenser lens (f=317.5 mm, effective diameter = 50.8 mm).

Figure 31 is the overall experimental setup for the demonstration of the spectral microscopy. The justification of wavelengths for RGB light sources are found in the section 1.8.1; specification of ① the collimating lens and ⑤ the field condenser lens are found in the section 1.8.2.1; dichroic mirrors are long passes with a cutoff frequency between red and green ③, and green and blue ④; the matching lens ② merely has the same focal length and diameter so that all three beams can enter and exit through dichroic mirrors without change in the diameter or the divergence angle; 10 ns of the light pulse was commanded by the pulse generator and the actual light pulse is measured; the WD and NA of the microscope are 228 mm and 0.083 respectively; the spray chamber radius is 222 mm; the spray is a water atomizer with expected droplet size <100 μm.

RESULTS AND DISCUSSION

8. Design of Spectral Microscopy Imaging System

1.8.1 Selection of Illumination Wavelengths

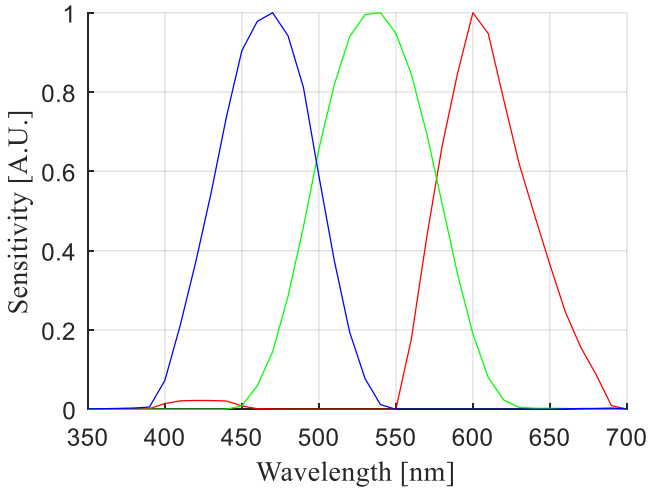

Figure 32 – Spectral sensitivity of Nikon D5300. LED wavelengths of 627 nm, 530 nm, and 447.5 nm were selected to avoid color crosstalk, while balancing maximum transmission near the peak detection sensitivity.

Figure 32 is the measured spectral sensitivity of the Nikon D5300 CMOS sensor over a range of wavelength. The sensitive range was 550 nm – 690 nm for the red, 450 nm – 630 nm for the green, and 390 nm – 550 nm for the blue. The peak sensitivity was observed at 600 nm, 535 nm, and 470 nm for RGB. Notice at peak sensitivity, there are overlaps especially for the blue and the red. LED wavelengths of 627 nm, 530 nm, and 447.5 nm were selected to avoid color crosstalk, while balancing maximum transmission near the peak detection sensitivity. Given that NA of the microscope is 0.083, the diffraction limited resolutions for the RGB color are 3.78 μm, 3.19 μm, and 2.70 μm, or 265 cyc/mm, 314 cyc/mm, and 370 cyc/mm.

1.8.2 Optical System Design

1.8.2.1 Selection of Condenser Lens

In Figure 33, the resolution comparison was made between the MTF measured with a collimated light source, and a NA matched light source. The resolution was measured at 10% of the MTF, as specified by ISO 12233. The resolution of the NA matched light source was measured as 224 cyc/mm; the resolution of the collimated light source was measured as 208 cyc/mm. There was not a significant difference between the MTF measured with collimated light source and the NA matched light source. It is speculated that this is because the collimated light has diverging

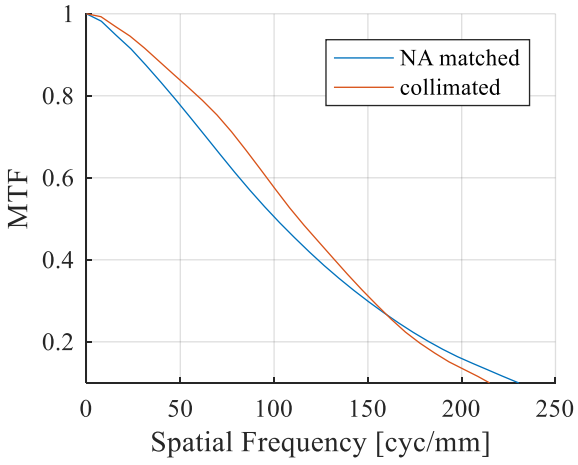

Figure 33 –MTF comparison of the NA matched light source, and the collimated light source. The resolution measured by MTF did not show a significant difference between NA matched and collimated configuration.

angle, which can be considered as an artificial NA. Even the ideally collimated LED light source has 1.34 degrees of diverging angle, calculated by the optical invariant (Eq. (13)), which corresponds to an NA of 0.023. Figure 34 is a visual comparison of the images taken with the NA

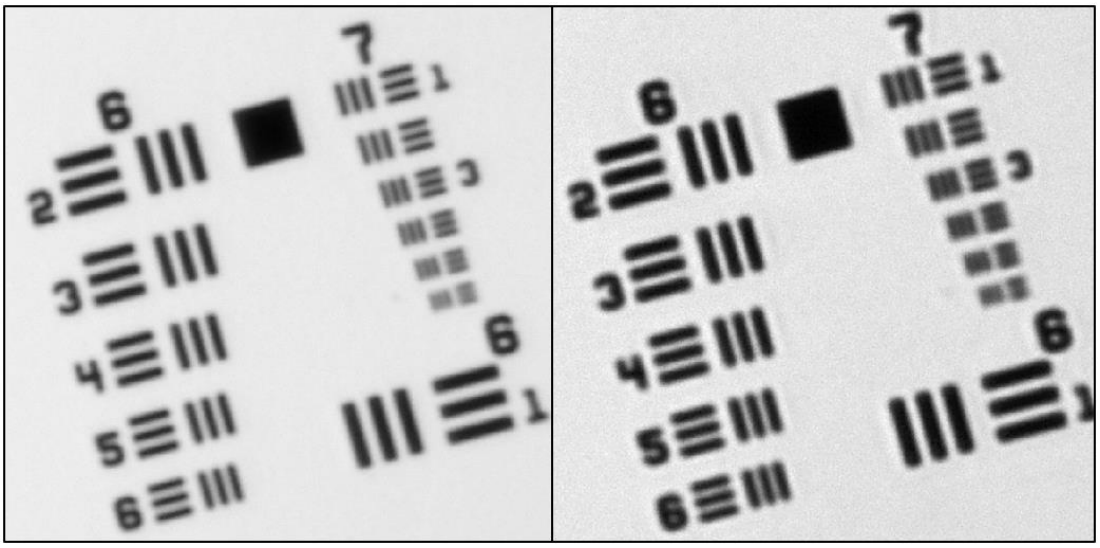

Figure 34 – Visual comparison of resolution target imaged with NA matched light source (left) and collimated light source (right)

matched light source and the collimated light source. The modulation of the NA matched light source target can be recognized as small as Group 7 Element 5 (203 cyc/mm), while the collimated light source target can be recognized down to Group 7 Element 3 (161.3 cyc/mm) but the entire shape is bolder than NA matched light source image (Figure 34).

1.8.2.2 Understanding Optical invariant and Selection of Collimating lens

An LED's optical power is much smaller than a laser's optical power. Furthermore, pulsing the LED in nano-seconds duration leads to lower optical power and a poor image contrast. To maximize the light throughput, illumination lenses need to be selected carefully. Simply using a collimating lens with the highest NA ensures the maximum amount of the light that can be collected from the light source, but this can also lead to another problem. Using a high NA collimating lens can create a larger spot size than the camera's field of view (FOV), which means any light out of the FOV will be wasted. The spot size at the focal plane is dependent on the first beam diverging angle created by the collimating lens [43, 44] such that the spot size is positively

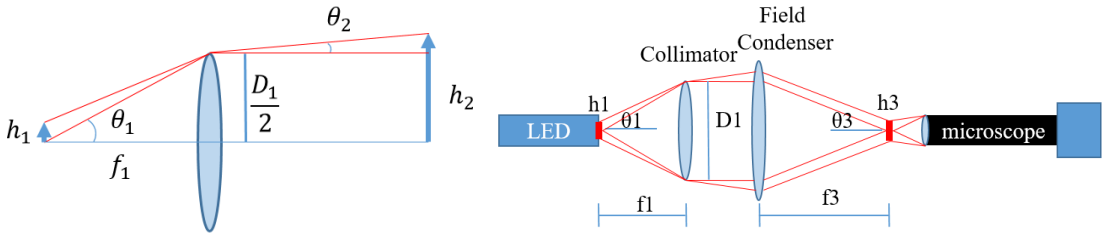

Figure 35 – Left: Diagram of Optical Invariant. Right: Diagram for simple two lens system.

correlated with the NA of the collimating lens. In other words, the spot size will grow as the NA of the collimating lens increases. The relationship between the NA of the collimating lens, light source, and spot size can be made by the optical invariant, which is a generalization of Lagrange invariant [43]. Equation (13) is the definition of optical invariant, which is using the fact that "in any optical system comprising only lenses, the product of the image size and ray angle is a

constant" [44]. Optical invariant can be re-organized (equation (14)) to derive an equation (15), which finds the spot size after two-lens system of Figure 35. Equation (13) through equation (16) can be used to find the optimized collimator and condenser lens dimension (Table 1). The f3 needs to be larger than the spray chamber radius, so 317.5 mm focal length Fresnel lens was used. h1 is the radius of the LED head. Table 1 shows that the spot size and the FOV are matched, as well as the $NA_{field\ condenser}$ and $NA_{objective}$ are matched.

$$h_1\theta_1 = h_2\theta_2, optical\ invariant\ [44] \tag{13}$$

$$h_1\left(\frac{\frac{D_1}{2}}{f_1}\right) = h_2\left(\frac{\frac{D_2}{2}}{f_2}\right), using\ small\ angle\ approximation\ and\ D_1 \approx D_2 \tag{14}$$

$$\frac{f_1}{h_1} = \frac{f_2}{h_2} \tag{15}$$

$$f\# = \frac{f}{D} = \frac{f}{2r} = \frac{1}{2\tan\theta} \tag{16}$$

Table 1 – Deriving the collimating lens dimension from the optical setup

Nomenclature	Definition	Value
f3	condenser lens focal length	317.5 mm
h1	LED head radius	0.75 mm
M	microscope magnification	5.6
Sensor Size	sensor Size	23.5 mm
FOV	$\frac{Sensor\ Size}{M}$	4.2 mm
h3 (spot size)	radius of FOV, and desired spot radius. $\frac{FOV}{2}$	4.19 mm
f1	equation (15) with f3 and h3	113 mm
NA (objective)	Microscope objective NA	0.083
θ3	arcsine (NA)	0.0831 rad
θ1	equation (13) With θ3 and h3	0.233 rad
f#1	equation (16)	2.15
D1	$\frac{f_1}{f\#_1}$	52.8 mm
NA_3 (field condenser)	$\frac{D_1}{2f_3}$, Field condenser NA	0.0831

To verify that the optimized collimating lens produces brighter image than the not-optimized high NA collimating lens, radiant flux comparison is made among three focal length collimating lenses with a focal length of 32 mm, 50 mm, and 125 mm. The rest of the dimensions were kept the same. The LED head manufacturer provides the relative luminous intensity by angle (Figure 36) and the

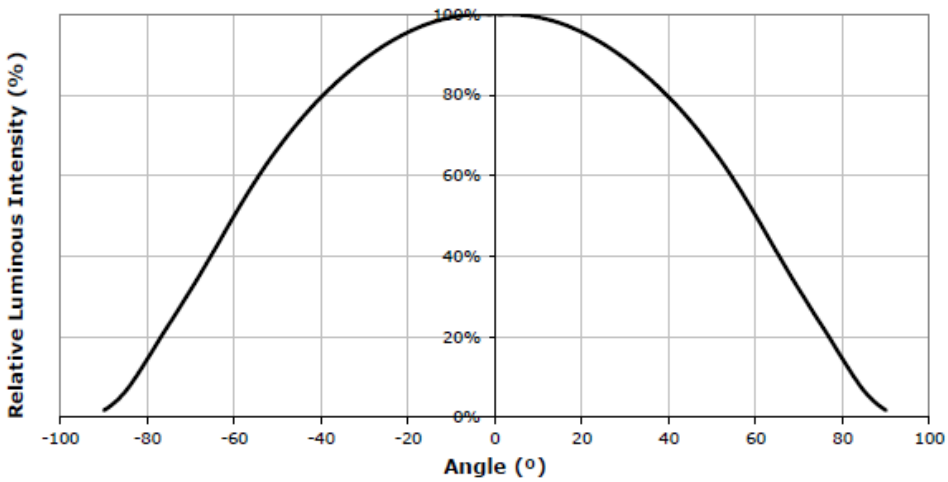

Figure 36 – Relative luminous intensity of an LED head as a function of angle, reproduced from [45]

entire area under the curve was assumed to be 1 W [45]. Table 2 is the comparison made for the three collimating lenses. Light captured is the area under the curve calculated with θ1 and Figure 36. h3 is the spot radius made by the three collimating lenses, and the irradiance is calculated by dividing the light captured by A3. Radiant flux is irradiance multiplied by the FOV of the camera

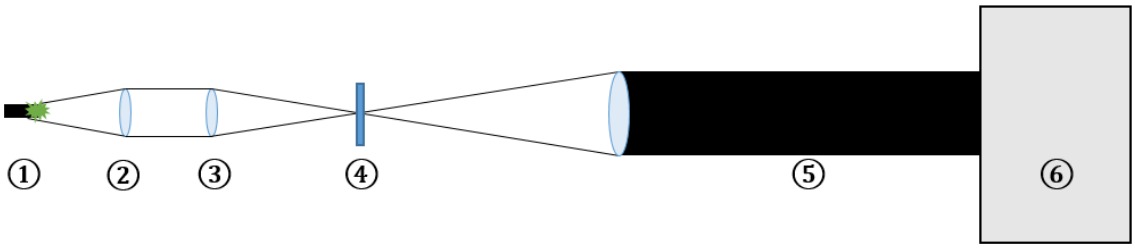

Figure 37 – Experiment setup to quntifying effectiveness of optimized field condenser includes, ① continuous white LED (5500K) light source, ② collimating lens D=50 mm, f=125 mm, 50 mm, and 32 mm ③ field condenser lens with D=10.4 in, f=12.5in, ④ USAF resolution target, ⑤ long distance microscope NA=0.083, and ⑥ Nikon D5300.

and representation of the expected brightness of the image. Table 2 radiant flux shows that the optimized lens with focal length 125 mm is expected to produce the brightest image of all three cases studied in Table 2. To verify the radiant flux with an experiment, a brightness comparison is made among the three collimating lenses. The experimental setup is as described in Figure 37. This experimental setup was written in this result and discussion section because it is more a part of discussion than a sole experimental setup. The collimating lens and its position is changed to re-collimate the light. The image of the LED head at the focal plane was captured with the camera, and average pixel intensities are compared. Contrast to the previously calculated radiant flux (Table 2), the relative pixel intensity was the highest for the collimating lens with shortest focal length, or the largest NA (Table 3). Modeling the experimental setup with Comsol or Zemax can analyze the reason for this unexpected phenomenon. Nevertheless, consequently for the final setup, the collimating lens with focal length 32 mm and diameter 50 mm was be used.

Table 2 – Radiant flux is correlated with the focal length of the collimating lens

Case	f1 (lens1)	h1 (LED)	Lens1 diameter (mm)	Lens1 radius (mm)	θ1 (degree)	Light captured (W)	θ3 (degree)	h3	A3 (mm^2)	Irradiance 10^{-3} $\left(\frac{W}{mm^2}\right)$	Radiant flux (W)
f32	32.0	0.75	50.0	25.0	38.0	0.69	4.57	6.2	121.9	5.6	0.10
f50	50.0	0.75	50.0	25.0	26.6	0.50	4.57	4.4	59.6	8.3	0.15
f125	125.0	0.75	50.0	25.0	11.3	0.22	4.57	1.9	10.8	20.0	0.35

Table 3 – Radiant flux verification

Collimating lens focal length (mm)	Collimating lens Diameter (mm)	Mean pixel intensity (cnt)	Relative pixel intensity	Relative radiant flux calculated
32	50	26127	1.00	0.10
50	50	22361	0.86	0.15
125	50	19276	0.74	0.35

9. Quantification of the Spectral Microscopy Image Resolution

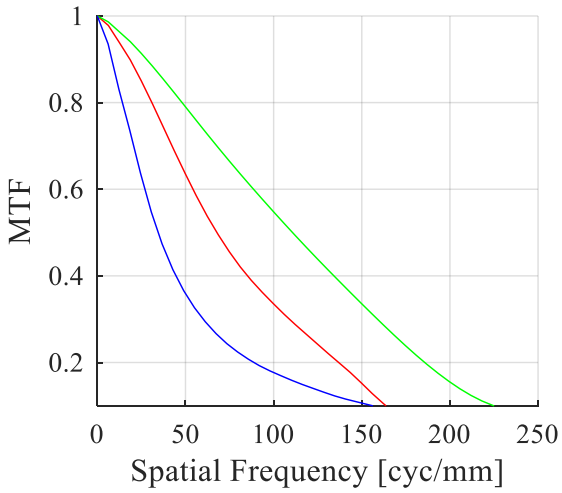

Figure 38 – RGB MTF plot at the final setup. To counter the chromatic aberration, each resolution was measured at each color's focal plane. The RGB resolution are measured as 162 cyc/mm, 224 cyc/mm, and 153 cyc/mm respectively.

MTFs were measured with ISO12233 e-SRF Code [33]. The RGB resolution are measured as 162 cyc/mm, 224 cyc/mm, and 153 cyc/mm respectively (Figure 38). The tailing behavior of the blue is a similar consequence of measuring the MTF from an image with noise (Figure 39) [46]. MTF is ultimately a FFT of an LSF. If the image is noisy, it causes noise to the LSF, which corresponds to a low MTF at a high frequency (cyc/mm) [46]. The tailing behavior can also come from defocus or aberration of the lenses inside of the microscope (Figure 40) [30]. Comparing the measured MTF (Figure 38) with the ideal MTF plotted with Clemens method (Abbe-MTF) (Figure

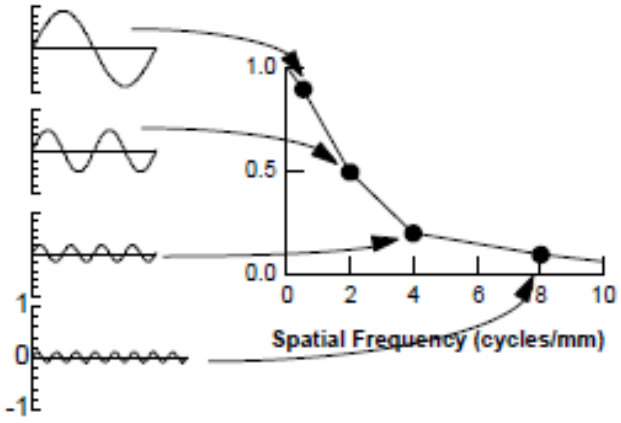

Figure 39 – Concept of measuring MTF. High frequency noise can cause a tailing effect of MTF plot [46].

41), shows disagreements in the order of the resolution superiority by colors [47]. Clemens method reflects the diffraction limited resolution, or Abbe criterion, which shows that the resolution increases with the decrease in wavelength. MTF plots with Clemens method will be referred as "Abbe-MTF" in this paper. For Figure 38, the green color has better resolution than the red or blue

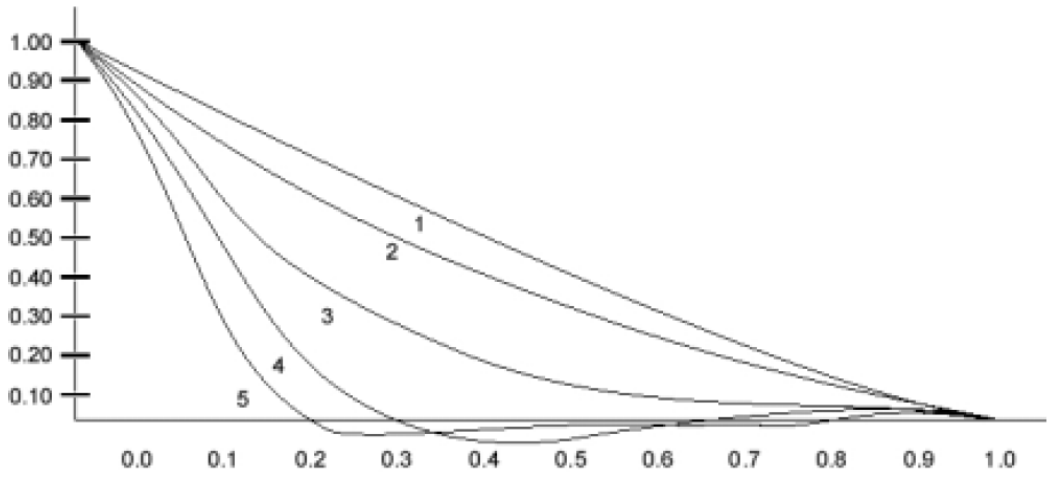

Figure 40 – MTF of a diffraction-limited lens at different amount of defocus. Increase in number 1-5 is increase in defocus. Figure reproduced from [30].

resolution because of the pixel count. Assuming the sensor is Bayer filter, green pixel count is twice as much as red or blue pixel counts in the camera which increases resolution; the blue color should have had a better resolution than the red resolution because the blue wavelength is shorter. There are two theories to explain these disagreements – the microscope design and the image sensor design. For the microscope design aspect, microscope's internal lens configuration needs to be considered. The long-distance microscope has an adjustable focus which changes its internal lens configuration to change its WD, NA, and magnification. Change in the lens configuration will change aberrations, which will have different impact on the MTF of each color. For instance, Figure 42 is a measured MTF plot at a different focus and magnification from the Figure 38. In this case, the measured RGB resolution was 65 cyc/mm, 66 cyc/mm, and 70 cyc/mm respectively. Notice how the superiority order has changed simply by changing the focus. For the image sensor design aspect, the Nikon D5300 CMOS sensor may have the different resolution solely depending

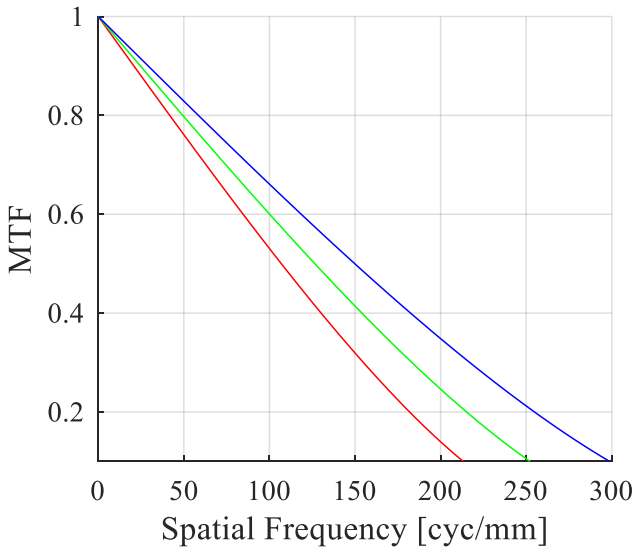

Figure 41 – Ideal diffraction-limited RGB MTF. The RGB resolution are measured as 210 cyc/mm, 250 cyc/mm, and 300 cyc/mm respectively. The methodology is studied by Clemens and will be referred to as Abbe-MTF in this paper [47].

on the incoming wavelength [48]. Djite et al. have characterized MTF of different image sensors, including CCD and CMOS [48]. They have found that decrease in the wavelength can also

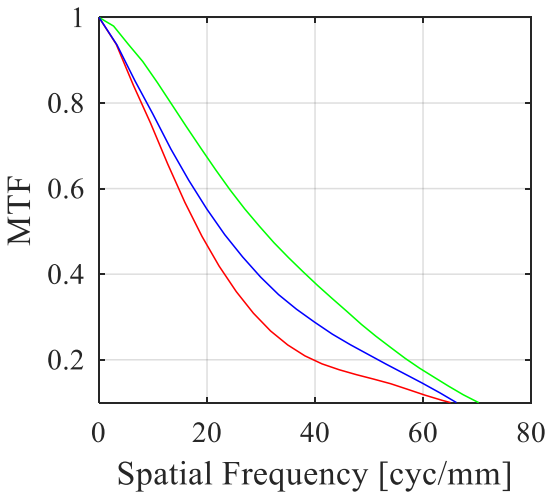

Figure 42 – MTF measured with the same microscope but a different focus

decrease the overall MTF for some image sensors [48]. This is caused by the wavelengths penetrating through the image sensor and causing the electrical cross-talk. Figure 43 shows the visual comparison between the green and blue images. The blue image shows what seems to be the electrical crosstalk. The blue image was not over saturated

Image resolution is measured with the ISO 12233 MTF method [33], Abbe-MTF [47], and Abbe diffraction limit. Abbe-MTF and Abbe diffraction limit estimates the ideal resolution, which

Table 4 - Resolution comparison by methods

Method	Red (cyc/mm)	Green (cyc/mm)	Blue (cyc/mm)
Abbe Criterion	265	314	370
Abbe-MTF	210	250	300
MTF (at best focus)	162	224	153

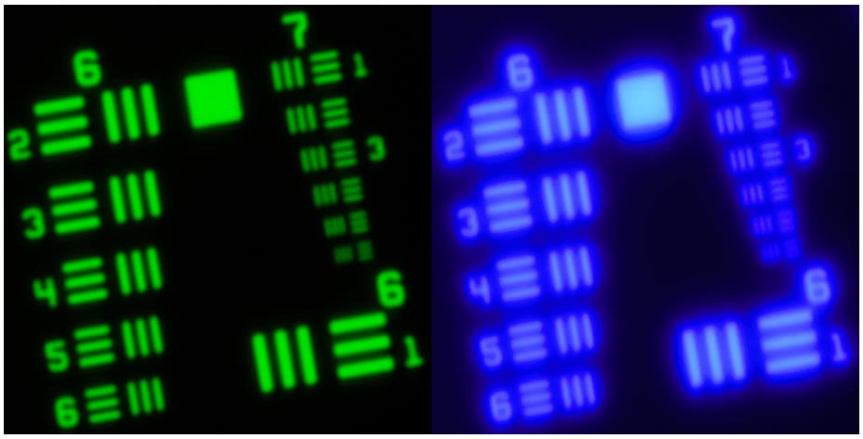

Figure 43 – Visual comparison of the resolution target. The blue image is in focus but shows bleeding, or pixel crosstalk, effect.

the resolution depends on the overall NA of the lens and wavelength of the light. Abbe-MTF defines the resolution at 10% of its MTF. Abbe criterion can be interpreted as when Abbe-MTF

reaches 0 of its MTF. MTF (not ideal like Abbe criterion or Abbe-MTF) measures the practical resolution, which the resolution depends on NA of the lens, wavelength of the light, lens design, and the image sensor [48, 49, 50]. Overall resolution comparison is made in Table 4. The resolution estimation by Abbe-MTF was generally 80% of the Abbe criterion diffraction limited resolution. The MTF values noted as “at best focus” were measured at each color’s focal plane, instead of at a single imaging plane. With the LCA and short pulsed light, the overall MTF will be lower. The measured MTF was less predictable because the MTF depends on the characteristics of the imaging equipment. The superiority of the resolution measured with MTF was in order of green, red, and blue.

10. Digital Color Imaging

1.10.1 ISO Sensitivity and Noise

In the spectral microscopy system developed in this thesis, the pulse duration of the light sources is as short as 10 nanoseconds, which produces low contrast images. Recall that previously in MTF section 1.5.2, it was mentioned that the contrast does not affect MTF - the measure of resolution. However, this is only true when no other types of noise are present. Low light can affect the resolution by adding photon noise, also known as the shot noise or quantum noise [51]. In equation (17) and equation (18), σ is photon noise, N is the number of incident photon to the

$$\sigma = \sqrt{N} \tag{17}$$

$$SNR = \frac{N}{\sigma} \tag{18}$$

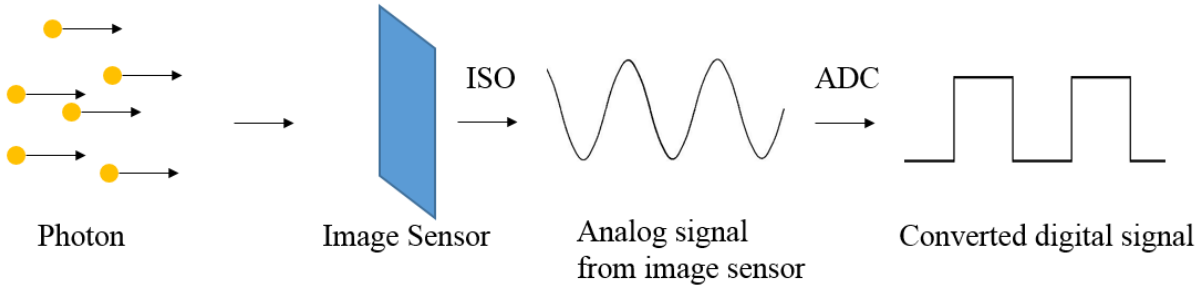

Figure 44 - Camera imaging process. Controlling the contrast with ISO sensitivity may amplify the photon noise from image sensor, but controlling the contrast with post-processing may amplify photon noise, ADC noise, and noises from the downstream electronic components.

sensor, and SNR is signal to noise ratio [51]. SNR increases with increase in the number of photon or amount of light. To overcome under illumination, higher ISO sensitivity may be used to amplify the light signal. Increasing the ISO sensitivity of a camera adds less noise than controlling the

contrast by post processing images. Figure 44 depicts the process of how photons from an object is converted to a digital signal through a camera. The ISO sensitivity increases the contrast by amplifying the analog signal that's created by an image sensor, while the post processing amplifies (or re-scales) the converted digital signal and any other downstream noises. Thus, increasing the ISO sensitivity only amplifies the photon noise while the post processing amplifies the photon noise, the read noise from an analog-to-digital converter (ADC), and the noise from any other downstream components. For this reason, the contrast should be increased with ISO sensitivity setting if the image is not saturated.

The impact of the ISO sensitivity is studied with images of a resolution test target, which each bar pattern can be considered as a knife edge, at different ISO sensitivities. The experimental setup is same as upper image of Figure 15. A 10 ns commanded light pulse illuminated the negative 1951 USAF resolution target, which can be considered as a large knife-edge. First, the dark portions of the images were compared to see the scale of the dark noise between low and high ISO sensitivities. Then, to compare the digital resolution, the dynamic range is compared between the high and low ISO sensitivity. The image of a knife edge can be considered as a simple ESF as shown in Figure 45. In the digital image, the analog knife-edge is digitized to a finite number of pixel intensities. Image A has more pixels than the image B in Figure 45, thus image A can be considered to have a higher digital resolution than image B. From the knife-edge image, the number of unique value is found in each image, and plotted against the ISO sensitivity setting. The dark noise from higher ISO sensitivity should not contribute to the number of the unique value, because ideally the ESF should include all possible pixel intensity values, even the noise.

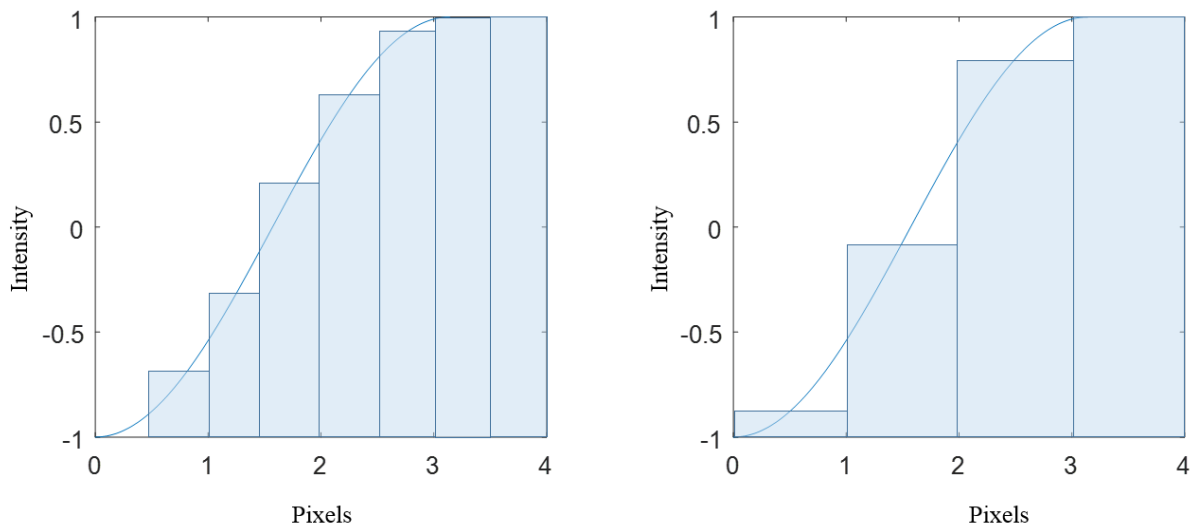

A B

Figure 45 – Example ESF digitized with A: 8 pixels and B: 4 pixels. A has higher pixel number and thus higher digital resolution.

Figure 46 is the image of the resolution test target with a 10-ns commanded pulsed green light, with re-scaled contrast. The lower ISO sensitivity image seems to have less background noise but with a price of a severe data loss. For the lower ISO image, the group 7 bar patterns are not discernable. Figure 47 shows the scale of the background noise in two systems. The highest ISO sensitivity image contains background noise, while the lowest ISO sensitivity image didn't. The mean of dark background noise was 0.75% of the full well capacity of the image sensor at the highest ISO sensitivity setting thus can be considered as insignificant. Figure 48 is the count of unique values within an image, across the ISO sensitivities. The test target image with ISO 100 had 133 unique values, and the image with ISO 25600 (the highest) had 15840 unique values. 133 and 15840 unique value are 0.81% and 97% of the entire image sensor full well capacity, each. While achieving 97% of the full well capacity, the high ISO did not oversaturate the image. Even

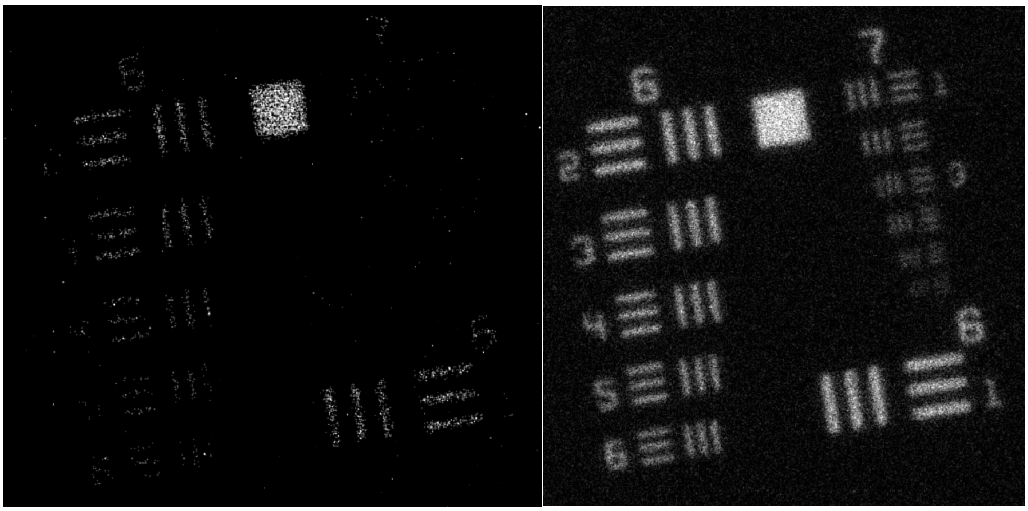

Figure 46 – Resolution test target imaged with ISO sensitivity 100 (left) and 25600 (right). Low ISO sensitivity image has less background noise but much of the data was lost.

at the highest ISO sensitivity setting, the mean pixel intensity of the fully illuminated portion of the image with 10 ns commanded light pulse was only 15%. Because the highest ISO sensitivity

had a bigger digital resolution, utilized more of the full well capacity, and did not saturate the image, the highest ISO sensitivity should be used for the demonstration experiment.

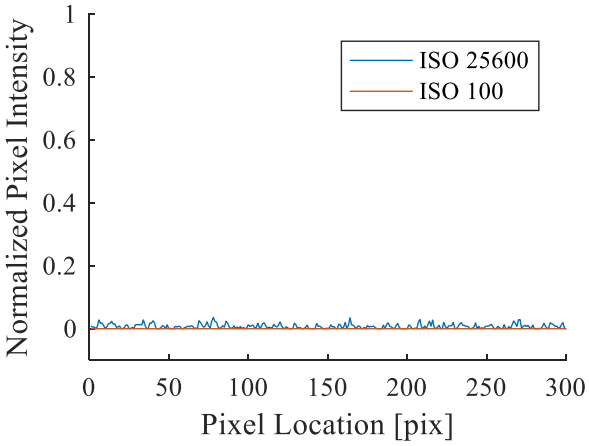

Figure 47 – Comparison of empty background pixel intensity between the high and low ISO sensitivity. Mean noise pixel intensity for ISO 25600 was 0.75% of the entire full well capacity.

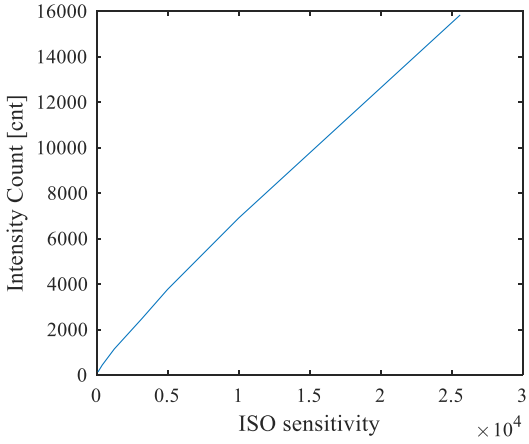

Figure 48 – Number of unique values, or intensity count, in the image of a knife edge at varying ISO sensitivity. The maximum number of intensity for the camera is 16,384.

1.10.2 Color Filter Array Pattern Results

The light sources are directly imaged at the corner of the camera FOV. The raw format of the image was read and the CFA mosaic pattern was visualized (Figure 49). The bright pixels represent the light transmitted pixels. The camera is confirmed to have a Bayer filter array with the "rggb" pattern, which has twice as many green pixels than the red or blue. The type of CFA, camera image sensor geometry, and magnification are found to define the Nyquist spatial resolution. The listed camera sensor size is 23.5 mm X 15.6 mm and the image size is 6000 pixel x 4000 pixel. This means that the pixel size is 3.92 μm or approximately 4 μm. Using the dimension of the pixel size, the pixel pitch can be found. The pixel pitch is defined as the distance between the two closest pixels of the same color. The pixel pitch for the red and blue color is 8 μm, and the pixel pitch for the green is 5.66 μm diagonally. The listed magnification of the overall setup is 5.6. With equation (11), the Nyquist limited spatial resolution for red and blue is found as 350 cyc/mm, and for green is 495 cyc/mm. The Nyquist spatial resolution and the optical resolution are the two criteria that defines the overall system resolution. The system resolution is less than whichever one of the two criteria is smaller [30]. Because the optical resolution is fixed at the setup, the spatial resolution needs to be equal or greater than the optical resolution to maximize the overall system resolution. The Nyquist limited spatial resolution is higher than the ideal diffraction limited optical resolution defined by Abbe-MTF (Table 4) [47]. The RGB resolution defined by the MTF is 46%,

45%, and 43% of the Nyquist limited spatial resolution, respectively. The overall system resolution is limited by the optical resolution and is maximum at the fixed WD.

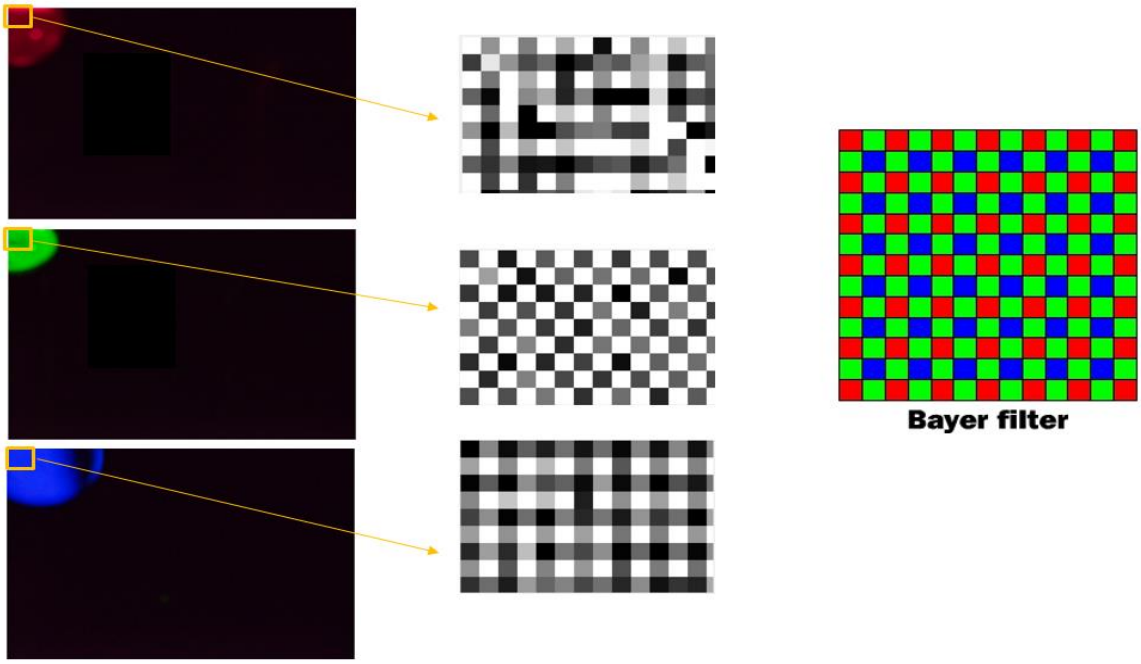

Figure 49 – Nikon D5300 CFA is a Bayer filter array

1.10.3 Longitudinal Chromatic Aberration (LCA) Results

Finding the focal plane with the frequency domain image quality measure (FM) suggested by De et al. is first validated by comparing with the modulation result [52]. Figure 50 shows that the FM is more sensitive to the image blur than the modulation, thus more accurately measuring the focal plane location. Additionally, FM is faster and simpler than measuring the modulation. FM is used to find the focal plane location, or WD, of the RGB (Figure 51). The red and green has the same focal plane location; the red and blue focal plane is 1 mm away from each other and thus the LCA is 1 mm. LCA affects the resolution if it is greater than the DOF of the system. The manufacturer listed DOF of the system is 80 μm and the overall chromatic aberration is 12.5 times of the DOF. Since the red focal plane and the green focal plane location are the same, the red and green images' resolution are not expected to suffer from the LCA, but the blue image's resolution will. Figure 52 is the MTF of the RGB color at green focal plane and 10 ns pulsed illumination, which is the final setup that is used in the section 1.10.5. The image blur caused by LCA also affects the apparent image size, which will be investigated in section 1.10.4.

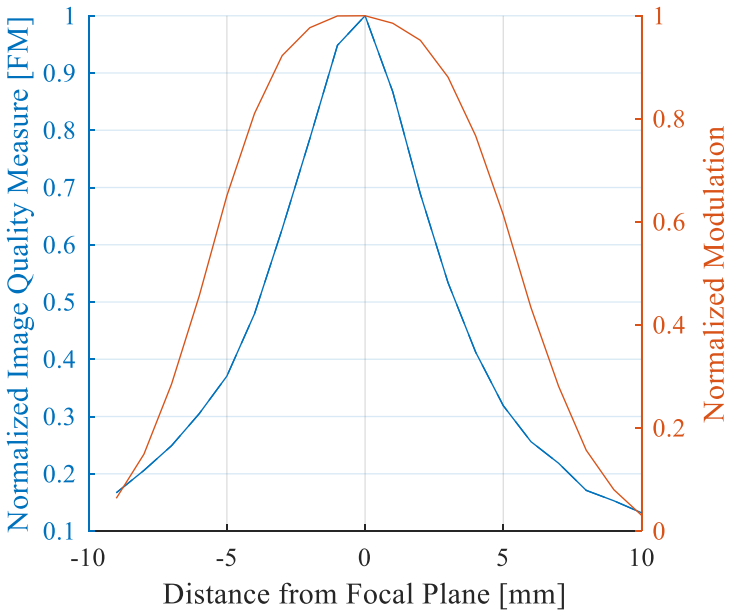

Figure 50 – Comparison of measuring blur with FM and modulation. FM is more sensitive to the blur and simpler to measure.

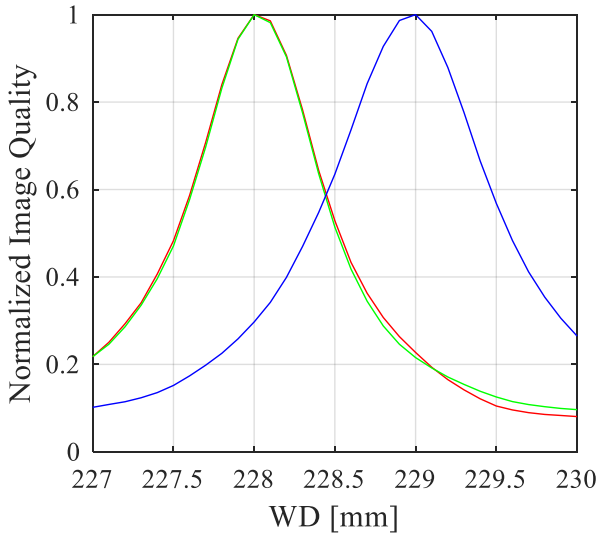

Figure 51 – Focal plane location and the LCA of the long-distance microscope at NA 0.083. The red and green has the same focal plane location, or WD, but the blue is 1 mm away from red and green. LCA is 1mm.

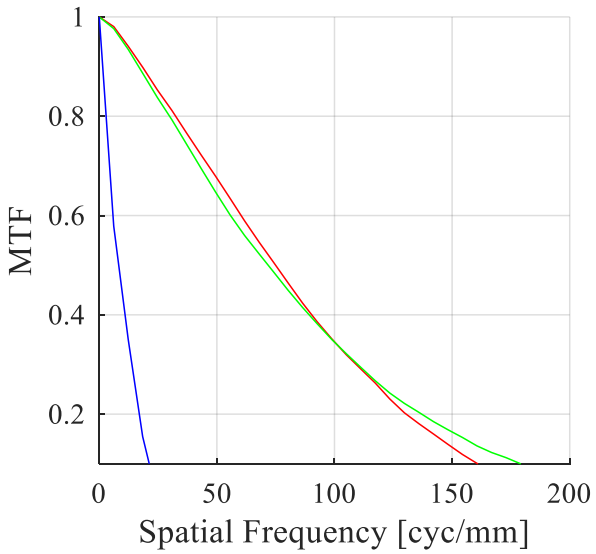

Figure 52 – MTF measured at the green focal plane and 10 ns commanded pulsed light. The resolution is measured as 160 cyc/mm, 178 cyc/mm, and 15 cyc/mm, respectively.

1.10.4 Size Error Caused by LCA

The apparent size of the 2227 µm square target was measured at every increment of 200 µm away from each color's focal planes (Figure 53). The square target appears as a quasi-step function at the exact focal plane and the slope of the sides gradually decreases as the image moves away from the focal plane. The FWHM at each WD was measured from Figure 53, and this is called as "apparent size." The difference between the focal plane apparent size and the out-of-focus apparent size is called "size error." Figure 54 plots the size error as a function of the distance away from the focal plane. The plot shows that the green's size error is more resistant, and blue is most affected by the image blur from out-of-focus than other colors. We speculate the green having twice as many pixel count has attenuated its size error, while blue having the shortest wavelength

and thus most shallow DOF worsened the size error [42, 53]. The plot also shows that the blue has at least 15 µm size error with 1 mm LCA. At each RGB focal plane, the measured target size was 2246 µm, 2244 µm, and 2240 µm respectively and the true target size was 2227 µm. There was a slight size difference even between the colors because the perceived light intensities for each color were different. Figure 53 shows that the peak normalized pixel intensity for blue was the highest and red was the lowest. The pixel intensity is a function of various factors such as the quantum efficiency of the CMOS sensor, the LED optical power efficiency, the color transmittance of the microscope, and the color transmittance of the Bayer filter. The object appears smaller in brighter back-light for a single beam illumination [42] and consequently, the apparent size at focal planes is high to low in the order of RGB.

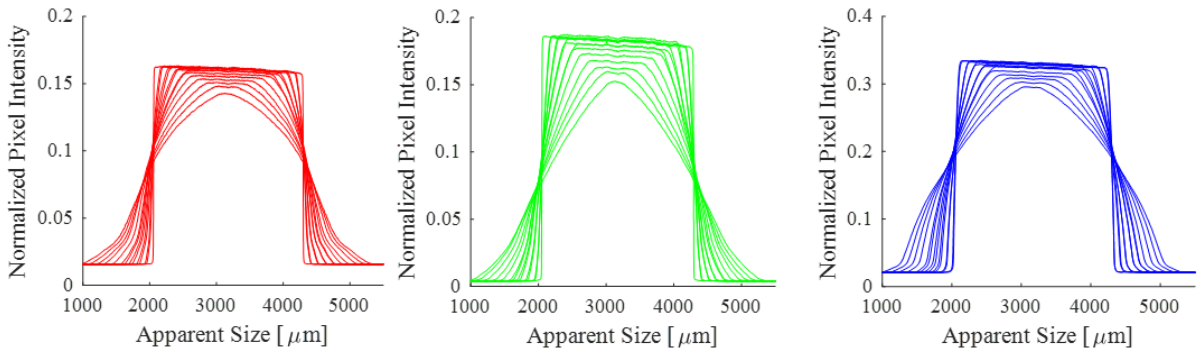

Figure 53 – Apparent size of a square target at a range of WD. Lower peak normalized pixel intensity causes the image to look larger in FWHM [42].

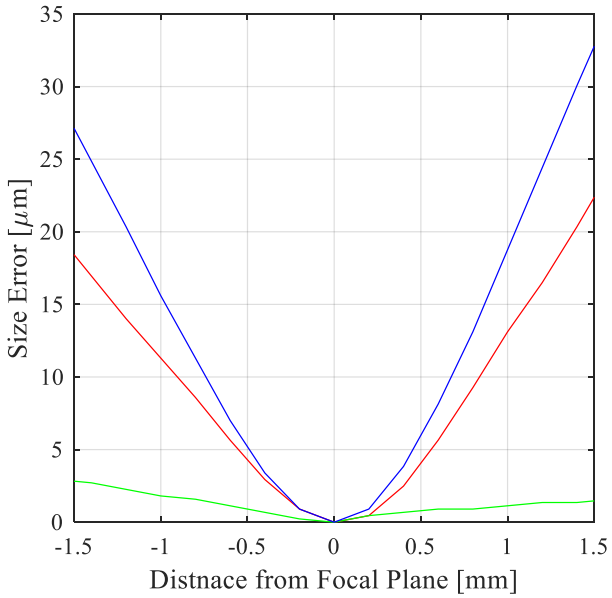

Figure 54 – Size error increases with the distance away from the focal planes. Blue color suffered most from the size error caused by out-of-focus blur.

1.10.5 Demonstration of Spectral Microscopy Applied to Water Spray

At a 10 ns commanded pulse, the RGB LED drivers produced average of 33 ns FWHM pulses (Figure 55). 10 ns commanded pulsed light was not enough to fully illuminate the image. Even at the highest ISO sensitivity, the mean pixel intensity of an image without spray is only 15% of the saturation. For this reason, images were taken with the highest ISO sensitivity setting to increase the contrast. The resolutions of the RGB color are 160 cyc/mm, 178 cyc/mm, and 15 cyc/mm respectively (Figure 52). The final resolution comparisons by different criteria is compared in Table 5. Figure 56 through Figure 59 are images of air assisted water atomizer at the

Table 5 – Final Resolution Comparison by Methods

Method	Red (cyc/mm)	Green (cyc/mm)	Blue (cyc/mm)
Abbe Criterion	265	314	370
Abbe-MTF	210	250	300
MTF (at best focus)	162	224	153
Nyquist Criterion	350	495	350
MTF (single image plane, pulsed illumination)	160	178	15

nozzle tip. The end of the nozzle is at just out of the top left corner and the water jet is propagating down-right direction. Each image has a colored circle scale. Black circle represents un-separated RGB image, and RGB colored circles represents RGB color channels. The sequence of the images was taken in the order of RGB, red being imaged first and blue imaged at last. The water jet speed was approximated as 9 m/s at the nozzle tip, by tracing the droplet. The red images seem more in-focus than the green images even though they had the same focal plane location. The longer wavelengths have the deeper depth of field, and it may have contributed in capturing better images [53]. The blue images suffered most from LCA caused out-of-focus, and there are even signs of lateral chromatic aberration. Figure 60 is an image of the resolution test target in the place of the water jet. The blue image is perceived to shifted up-right direction.

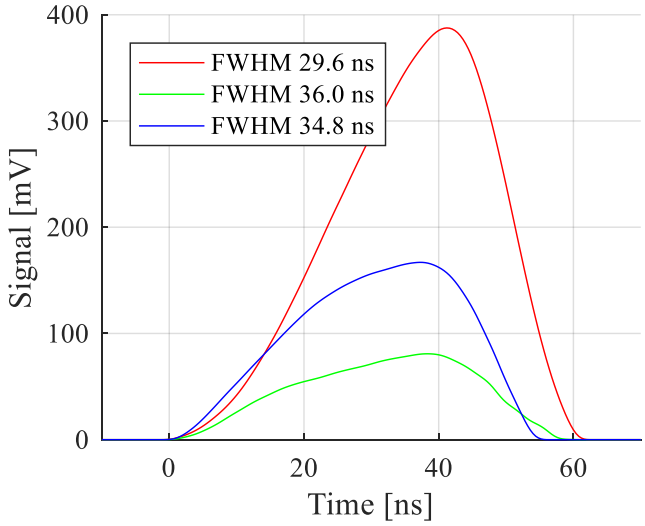

Figure 55 – Light pulse duration at 10 ns commanded signal. The average light pulse duration is 33 ns.

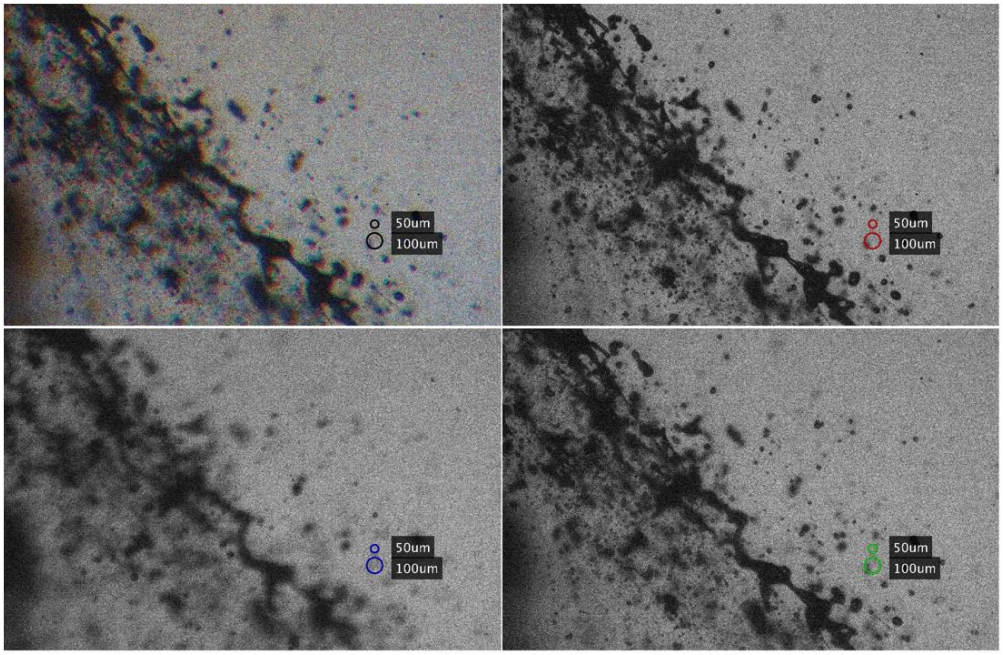

Figure 56 – Frame rate: 1Mfps; shutter duration: 33 ns

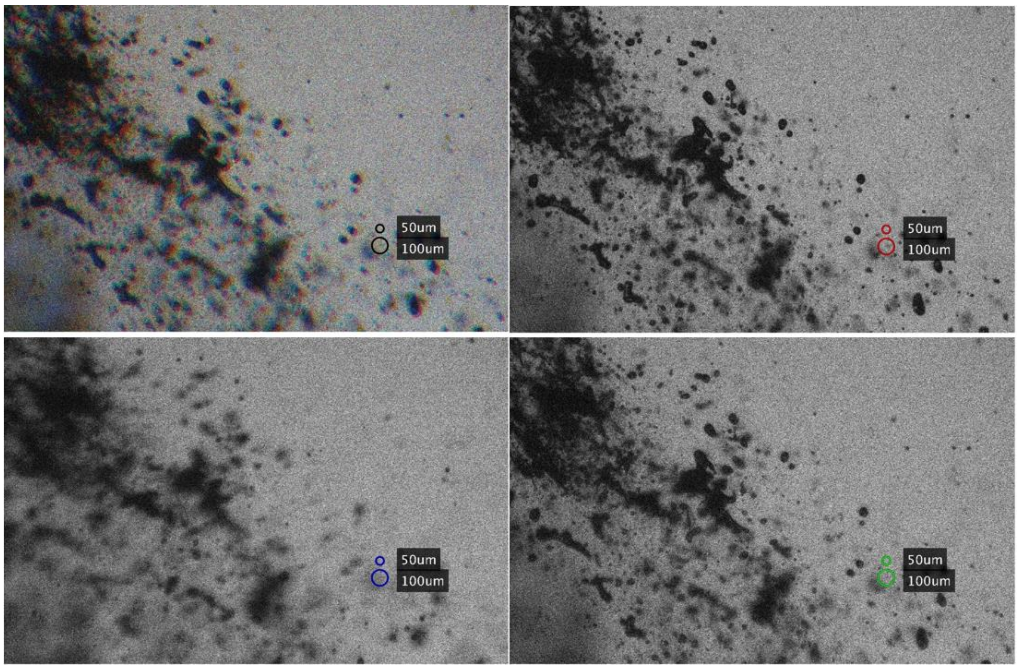

Figure 57 – Frame rate: 1Mfps; shutter duration: 33 ns.

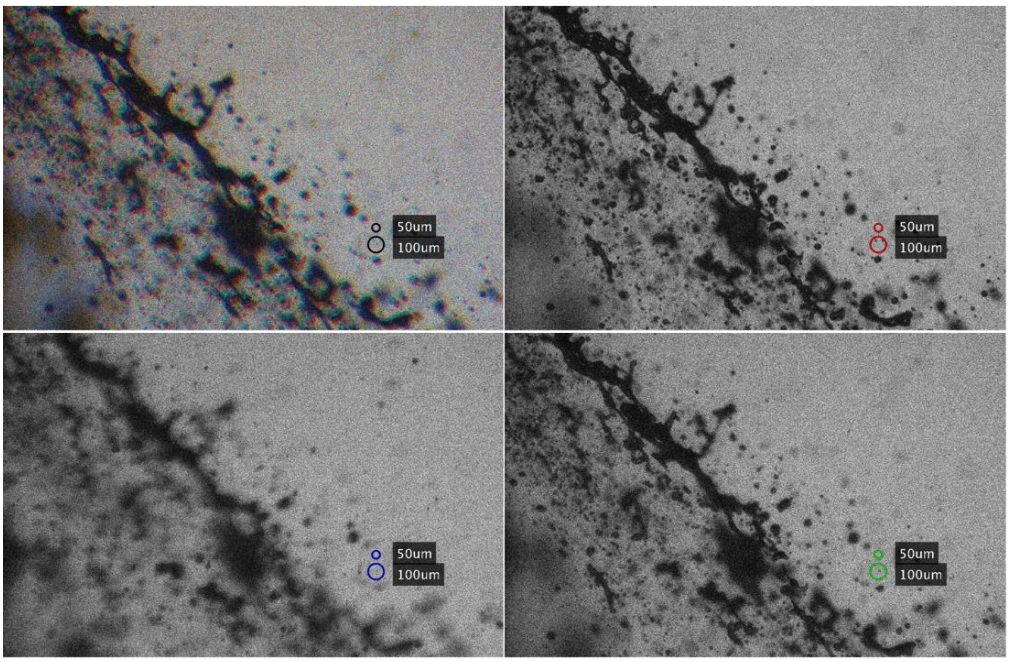

Figure 58 – Frame rate: 1Mfps; shutter duration: 33 ns.

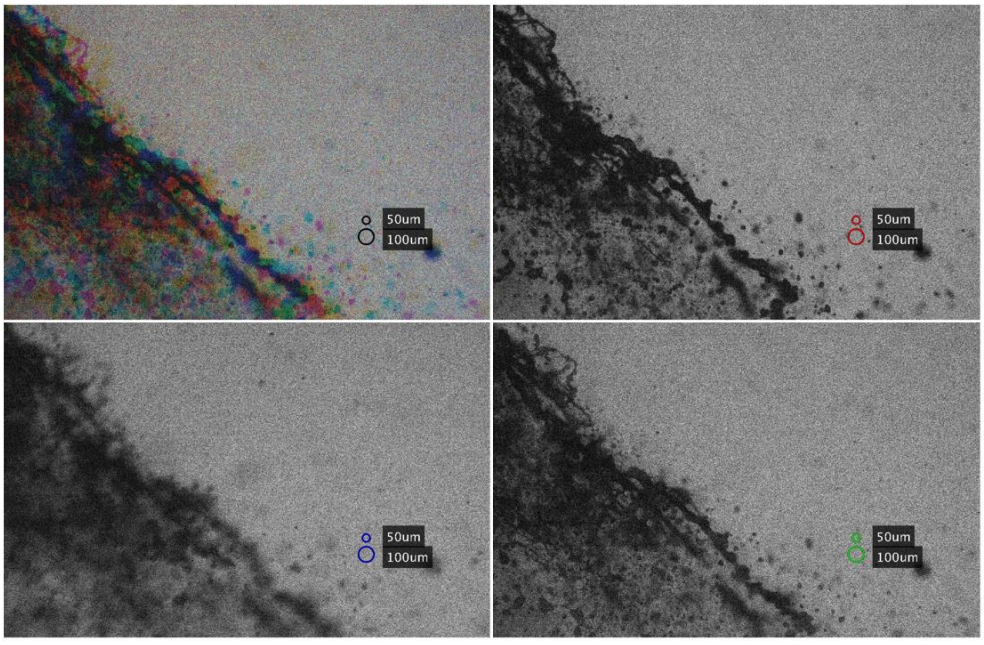

Figure 59 – Frame rate: 200 kfps; shutter duration: 33 ns.

Figure 60 – Resolution target imaged with all RGB color with a sign of lateral chromatic aberration for blue. The blue image is shifted to up-right direction.

11. Conclusion and Future Work

The concept of the spectral microscopy was built and tested. The imaging system had resolutions of 160 cyc/mm, 178 cyc/mm, and 15 cyc/mm for RGB color or the observable object size of 6.25 µm, 5.62 µm, and 66.7 µm; the average minimum shutter (light pulse) duration was 33 ns; the pulse generator can output a pulse separation minimum of 10 ns and this led to an ideal framerate of 100 Mfps; the minimum FWHM of light pulse is 33 ns and this led to a practical framerate of 30 Mfps; the LCA was 1 mm and it led to approximately 17 µm of the blue channel size error; the useful range of the 14-bit camera sensor is 16384 pixel intensity and 96% of the total pixel intensity was utilized with the highest ISO sensitivity but with a cost of an amplified

noise; mean pixel intensity with 10 ns commanded light pulse without an object was only 15% of the full well depth even at the highest ISO sensitivity.

The system can mainly be improved by a lower LCA, a higher camera frame rate, and a stronger and faster light source. For the LCA, a macro lens can be used. Macro lenses cannot adjust its focus but they are able to mitigate most of aberrations, including LCA. For the camera framerate, the current DSLR camera can only take an image per a second and a burst of only 3 images at 100 Mfps with the RGB illumination. Scientific high-speed cameras can achieve kilo-frames-per-second rate which can increase the overall frame rate. For the better light source, either laser diodes or speckle free lasers can be used. An optical merchandise company Thorlabs have nanosecond pulsed laser diode systems, which has pulse width of longer than 6 ns at a repetition rate 10 MHz. The peak optical power of the laser diode may not be much higher than that of the current high-power LED system, but the laser diode can achieve shorter pulse width (6 ns – 40 ns) and faster rise of light intensity (< 5 ns). Laser diodes generally do not produce speckles. In case of laser systems, some are equipped with speck attenuation system. Speckle-free laser system can improve the image contrast with an extremely high optical power output by allowing a low ISO sensitivity setting, and higher SNR.

GLOSSARY

α	Angular aperture
cyc/mm	Cycle per millimeter
CFA	Color filter array
CTF	Contrast transfer function
DOF	Depth of field
DSLR	Digital single-lens reflex
f#	F-number
FM	Frequency domain image blur measure
FOV	Field of view
FWHM	Full width half maximum
M	Magnification
MTF	Modulation transfer function
NA	Numerical aperture
RGB	Red green blue
SNR	Signal to noise ratio
WD	Working distance

REFERENCES

[1] J. P. Valentine, "EPA Sets Cleaner Fuel and Car Standards, Slashing Air Pollution and Providing Health Benefits to Thousands," 2014. [Online]. Available: https://yosemite.epa.gov/opa/admpress.nsf/bd4379a92ceceeac8525735900400c27/ce8984957ffefa6a85257c90004fe802!OpenDocument. [Accessed 2017].

[2] U. S. E. P. Agency, "Inventory of U.S. Greenhouse Gas Emissions and Sinks," 2017.

[3] U. E. I. Administration, "Annual Energy Outlook 2017," 2017.

[4] U. D. o. Energy, "Advanced Combustion Systems and Fuels," [Online]. Available: https://energy.gov/eere/vehicles/advanced-combustion-systems-and-fuels. [Accessed July 2017].

[5] M. Dale, "The fuel economy solution? gasoline direct injection," 07 2009. [Online]. Available: https://www.motor.com/magazine-summary/the-fuel-economy-solution-gasoline-direct-injection/. [Accessed 10 2017].

[6] A. Kastengren, J. Ilavsky, J. Pablo Viera, R. Payri, D. J. Duke, A. Swantek, F. Zak Tilocco, N. Sovis and C. F. Powell, "Measurements of droplet size in shear-driven atomization using ultra-small angle x-ray scattering," *International Journal of Multiphase Flow*, pp. 131-139, 2017.

[7] R. D. Reitz and F. V. Bracco, "Mechanism of atomization of a liquid jet," *Phys. Fluids*, pp. 1730-1742, 1982.

[8] R. D. Reitz and F. V. Bracco, "On the Dependence of Spray Angle and Other Spray Parameters on Nozzle Design and Operating Conditions," *SAE Technical Paper Series*, 1979.

[9] K. A. Sallam and G. M. Faeth, "Surface Properties During Primary Breakup of Turbulent Liquid Jets in Still Air," *AIAA*, 2003.

[10] K. A. Sallam, Z. Dai and G. M. Faeth, "Drop Formation at the Surface of Plane Turbulent Liquid Jets in Still Gases," *International Journal of Multiphase Flow*, pp. 1161-1180, 1999.

[11] S. Som and S. K. Agarwal, "Assessment of Atomization Models for Diesel Engine Simulations," *Atomization and Sprays*, vol. 19, no. 9, pp. 885-903, 2009.

[12] P. K. Wu, L. K. Tseng and G. M. Faeth, "Primary Breakup in Gas/Liquid Mixing Layers for Turbulent Liquids," *Atomization and Sprays,* pp. 295-317, 1992.

[13] C. Crua, M. R. Heikal and M. R. Gold, "Microscopic imaging of the initial stage of diesel spray formation," *Fuel,* vol. 157, pp. 140-150, 2015.

[14] J. Manin, L. M. Pickett and C. Crua, "Microscopic observation of miscible mixing in sprays at elevated temperatures and pressure," in *ILASS Americas,* Raleigh, 2015.

[15] T. Lian, S. Wang, D. Cai, B. Li and Z. Guo, "High repetitionrate,highpeakpower,pulsed single-longitudinal-mode Nd:YAGlaserbyself-injection-seeding," *Optics Communications,* pp. 154-161, 2014.

[16] J. W. Goodman, "Some fundamental properties of speckle," *The Journal of the Optical Society of America,* vol. 66, no. 11, 1976.

[17] J. Dainty, Laser Speckle and Related Phenomena, Springer, 1975.

[18] B. Redding, M. Choma and H. Cao, "Speckle-free laser imaging using random laser illumination," *Nature Photonics,* vol. 6, 2012.

[19] S. Jain, S. Somasundaram and T. N. C. Anand, "A fluorescent laser-diffuser arrangement for uniform backlighting," *Journal of Optics,* vol. 27, 2016.

[20] J.-W. Pan and C.-H. Shih, "Speckle noise reduction in the laser mini-projecor by vibrating diffuser," *Journal of Optics,* vol. 19, 2017.

[21] L. M. Pickett and J. Manin, "Comparison of Near-Field Structure and Growth of a Diesel Spray Using Light-Based Optical Microscopy and X-Ray Radiography," vol. 7, no. 2, 2014.

[22] R. D. Reitz, "Atomization and other breakup regimes of a liquid jet," Ph.D. Thesis Princeton Univ., 1978.

[23] B. E. Bayer, "Color imaging array". USA Patent US 3971065 A, 20 07 1976.

[24] Rensselaer Polytechnic Institute, "Spectral Response," 2004. [Online]. Available: http://www.lrc.rpi.edu/programs/NLPIP/tutorials/photosensors/spectral.asp. [Accessed 2017].

[25] F. Sigernes, M. Dyrland, N. Peters, D. A. Lorentzen, T. Svenøe, K. Heia, S. Chernouss, C. S. Deehr and M. Kosch, "The absolute sensitivity of digital colour cameras," *Optics Express,* vol. 17, no. 22, 2009.

[26] G. E. Blackham, On angular aperture of objectives for the microscope, Indianapolis: Industrial Publication Co., 1880.

[27] Nature Photonics Editorial, "Beyond the diffraction limit," *Nature Photonics,* vol. 3, no. 7, 2009.

[28] F. L. Pedrotti, L. M. Pedrotti and L. S. Pedrotti, Introduction to Optics, Pearson, 2014.

[29] M. Abramowitz, "Microscope Basics and Beyond," Olympus America Inc., Melville, NY, 2003.

[30] Optikos Corporation, "How to Measure MTF and other Properties of Lenses," Optikos Corporation, Wakefield, 1999.

[31] K. R. Spring and M. W. Davidson, "Nikon MicroscopyU - Modulation Transfer Function," 2016. [Online]. Available: https://www.microscopyu.com/microscopy-basics/modulation-transfer-function. [Accessed 2016].

[32] E. Hecht, Optics, Addison-Wesley, 2001.

[33] ISO, International Organization for Standardization, "ISO 12233, photography - electronic still picture imaging - resolution and spatial frequency response," Geneva, 2017.

[34] J. K. Roland, "A Study of Slanted-Edge MTF Stability and Repeatability," Imaest LLC, Boulder.

[35] M. Estribeau and P. Magnan, "Fast MTF measurement of CMOS imagers using ISO 12233 slanted-edge methodology," in *SPIE Optical System Design*, Saint-Etienne, France, 2003.

[36] D. A. Kerr, "Determining MTF with a Slant Edge Target," 2010.

[37] H. H. Nasse, "How to Read MTF Curves," Carl Zeiss, 2008.

[38] J. B. Pawley, Handbook of Biological Confocal Microscopy Third Ed., New York: Springer, 2006.

[39] R. Sumner, "Processing RAW images in MATLAB," UC Santa Cruz, 2014.

[40] S. Eddins, "Tips for reading a camera raw file into MATLAB," 2011. [Online]. Available: http://blogs.mathworks.com/steve/2011/03/08/tips-for-reading-a-camera-raw-file-into-matlab/. [Accessed 2017].

[41] K. De and V. Masilamani, "Image Sharpness Measure for Blurred Images in Frequency Domain," in *International Conference on Design and Manufacturing*, 2013.

[42] W. D. Bachalo, G. Payne, K. Ibrahim and R. Karami, "Multi-Beam Illumination for Coping with Dense Spray Using Imaging," in *ILASS-Americas*, Atlanta, 2017.

[43] J. E. Greivenkamp, Field Guide to Geometrical Optics, Bellingham: Spie Press, 2004.

[44] Newport Corporation, "Technical Note: Optics Fundamentals," [Online]. Available: https://www.newport.com/n/optics-fundamentals. [Accessed 2016].

[45] Cree, "ledsupply," [Online]. Available: http://www.ledsupply.com/content/pdf/leds-cree-xpg2_documentation.pdf. [Accessed 2017].

[46] R. M. Nishikawa, "The Fundamentals of MTF, Wiener Spectra, and DQE," in *American Association of Physicists in Medicine*, Nashville, TN, 1999.

[47] N. T. Clemens, "Flow Imaging," in *Encyclopedia of Imaging Science and Technology*, John Wiley & Sons, Inc., 2002, pp. 390-419.

[48] I. Djite, M. Estribeau, P. Magnan, G. Rolland, S. Petit and O. Saint-Pe, "Theoretical evaluation of MTF and charge collection efficiency in CCD and CMOS image sensors," *SPIE*, p. 12, 2009.

[49] I. Djite, P. Magnan, M. Estribeau, G. Rolland, S. Petit and O. Saint-Pe, "Modeling and measurements of MTF and quantum efficiency in CCD and CMOS image sensors," *SPIE-IS&T*, vol. 7536, 2010.

[50] M. Estribeau and P. Magnan, "CMOS pixels crosstalk mapping and its influence on measurements accuracy for space applications," *SPIE*, 2005.

[51] J. T. Bushberg, J. A. Seibert, E. M. Leidholdt and J. M. Boone, The Essential Physics of Medical Imaging, Lippincott Williams & Wilkins, 2001.

[52] K. De and V. Masilamani, "Image Sharpness Measure for Blurred Images in Frequency Domain," in *IConDM*, 2013.

[53] C. P. Shillaber, Photomicrography in Theory and Practice, New York: John Wiley and Sons, 1944.

[54] S. Tanguy, *Developpement d'une methode de suivi d'interface. Applications aux ecoulements diphasiques.*, Universite de Rouen, France, 2004.

[55] H. Gen Fugimoto, T. Hori, J. Senda, H. Nakagawa, S. Kamata and K. Katsuta, "Visualization of Micro Structure in a Diesel Spray by Use of Photography with High Spatial Resolution," *SAE International*, 2008.

[56] C. R. Bagnell Jr., *Light Microscopy - Lenses*, University of North Carolina at Chapel Hill School of Medicine, 2013.

[57] E. Abbe, "Beitrage zur Theorie des Mikroskops und der mikroskopischen Wahrnehmung (Contribution to the theory of the microscope and microscopic perception)," *Archiv für mikroskopische Anatomie,* vol. 9, no. 1, pp. 413-418, 1873.

[58] R. Nave, "HyperPhysics," Georgia State University, [Online]. Available: http://hyperphysics.phy-astr.gsu.edu/hbase/phyopt/sinslit.html. [Accessed 2017].